

Multiplex Nodal Modularity: A novel network metric for the regional analysis of amnesic mild cognitive impairment during a working memory binding task

Avalon Campbell-Cousins^{1*}, Federica Guazzo², Mark Bastin³, Mario A. Parra⁴, Javier Escudero^{1*}

1 School of Engineering, Institute for Imaging, Data and Communications, University of Edinburgh, Edinburgh, Scotland, United Kingdom

2 Human Cognitive Neuroscience, Psychology, University of Edinburgh, Edinburgh, Scotland, United Kingdom

3 Centre for Clinical Brain Sciences, University of Edinburgh, Edinburgh, Scotland, United Kingdom

4 Department of Psychology, University of Strathclyde, Glasgow, Scotland, United Kingdom

* Avalon.Campbell-Cousins@ed.ac.uk; Javier.Escudero@ed.ac.uk

Abstract

Modularity is a well-established concept for assessing community structures in various single and multi-layer networks, including those in biological and social domains. Biological networks, such as the brain, are known to exhibit group structure at a variety of scales – local, meso, and global scale. Yet, it is at this mesoscale level, between that of individual nodes and global network scales, where community structure can be observed. Changes at the mesoscale of the human brain have been observed in a wide range of studies. However, modularity, while useful in describing mesoscale brain organization, is limited as a metric to a global scale describing the overall strength of community structure. This approach, while valuable, overlooks important localized variations in community structure at the node level. To address this limitation, we extended modularity to individual nodes. This novel measure of nodal modularity (nQ) captures both meso and local scale changes in modularity. We hypothesized that nQ illuminates granular changes in the brain due to diseases such as Alzheimer’s disease (AD), which are known to disrupt the brain’s modular structure. We explored nQ in multiplex networks of a visual short-term memory binding task in fMRI and DTI data in the early stages of AD. Observed changes in nQ in fMRI and DTI networks aligned with known trajectories of AD and were linked to common biomarkers of the disease, including amyloid- β and tau. Additionally, nQ clearly differentiated MCI from MCI converters showing indications that nQ may be a useful diagnostic tool for characterizing disease stages. Our findings demonstrate the utility of nQ as a measure of localized group structure, providing novel insights into temporal and disease related variability at the node level. Given the widespread application of modularity as a global measure, nQ represents a significant advancement, providing a granular measure of network organization applicable to a wide range of disciplines.

Introduction

Alzheimer's disease (AD) and several other dementias often develop from Mild Cognitive Impairment (MCI) [1,2]. MCI is defined as a cognitive decline which is greater than that caused by normal aging [1]. While not everyone with MCI goes on to develop dementia, those with MCI are at much greater risk. MCI diagnosis is typically achieved through a collection of cognitive questionnaires, screening tests, and neuropsychological examinations [3], which are used to benchmark and assess changes in memory, visuo-spatial ability, language, and behaviour. For individuals presenting with the amnesic (memory-related) subtype of MCI (aMCI), this progression frequently results in AD, thereby leading aMCI to often be considered a prodromal stage of the disease [2]. Those who have a diagnosis of aMCI and who convert to AD (MCI converters) typically do so at a conversion rate of 12% per year [4].

Recent studies of AD biomarkers have presented significant promise in improving diagnosis and our understanding of disease progression. Some examples of this are biomarkers for several types of proteins and their accumulation in the brain (most notably amyloid- β and tau) and neurodegeneration markers from volumetric magnetic resonance imaging (MRI) [3,5,6]. These, among other biomarkers, have been tracked along the AD continuum from preclinical changes in amyloid- β deposition, to large changes in hippocampal volume toward the later stages of disease [5]. Furthermore, some biomarkers, such as amyloid- β and tau, can be assessed at a brain regional level allowing for improved staging of disease severity. For instance, research suggests that, for amyloid-positive subject groups, that amyloid deposition is most strongly found in the heteromodal association areas of the frontal, parietal, and lateral temporal lobes [7]. This begins in the preclinical stages (for amyloid positive subjects), increases through the pre-dementia stages (early to late MCI) and presents most strongly in AD. Evidence also points to the medial temporal lobe (MTL) as a key region in early-stage AD both in grey matter atrophy [7], and in functional activity [8]. Studies suggest that the AD continuum begins with damage to the MTL followed by broader damage to other networks such as those part of the frontal lobe [9–11]. While the combination of biological biomarkers, neuropsychological tests, and genetic risk markers can allow us to pinpoint the progression of MCI to AD with high accuracy [12,13], methods with higher specificity that explore how individual regions drive this change are needed. This motivates the development of novel biomarkers for AD, especially those sensitive to the early-stages of disease, where less damage has been done.

One such accepted neurocognitive biomarker is the Visual Short-Term Memory Binding Task (VSTMBT), introduced by Parra *et. al.* [14]. It is a task sensitive to early changes in AD, and is composed of eight non-nameable shapes and colours with three phases named encoding, maintenance, and probe. The VSTMBT targets visual memory binding in the brain, a process responsible for the temporary retention of complex objects (i.e., coloured shapes). In addition, tasks which target short-term memory binding are especially important for AD given that they remain relatively unchanged with age while being highly sensitive to the disease [14]. This sensitivity is specific to AD where conjunctive short-term memory binding (i.e., between colour and shape) is impaired as opposed to other, non-AD, dementias where this effect is not observed [15]. This evidence suggests that deficits in short-term memory binding is a preclinical marker of AD.

Using neuroimaging methods such as functional MRI (fMRI) or Electroencephalography (EEG), the dynamics in brain activity during a cognitive task, like the VSTBMT, can be measured. As AD progresses, changes in functional brain activity has been associated with lower brain efficiency and reduced functional connectivity between brain sub-networks, leading to the naming of AD as a disconnection syndrome [16–18]. This has been further explored in measures of

white-matter density and microstructure, measured using Diffusion Tensor Imaging (DTI) [19]. For instance, in [17], white matter structures in the frontal and temporal lobes are found to be vulnerable in early-stage damage caused by familial AD with associated impairments in memory-binding.

A natural model for this is to view the brain as a network to explore how connectivity changes with disease. In network neuroscience, networks typically model brain regions as nodes and the connections (edges) between them encode information on the relationship between those regions' function (functional connectivity) or structure (structural connectivity) [20]. In the case of fMRI, edges are often a measure of functional co-activation between blood oxygen level dependent (BOLD) time-series of a pair of brain regions [21]. Meanwhile, in DTI, an edge typically represents the fractional anisotropy (FA) between regions (measuring white matter micro-structure), or streamline density (white matter density) [22]. These models capture brain topology, revealing fundamental insights into how the brain is functionally and structurally organized, and how this changes due to disease.

More recently, this approach has been extended to multiplex networks in order to capture additional complexity. Multiplex networks, a type of multi-layer network, consist of multiple single-layer networks (each with the same number of nodes) where the connections within each layer describe a different type of interaction [23]. For instance, multiplex brain networks can be modelled with each layer representing windows of time in an fMRI scan or individual frequency bands in EEG [24]. In this way, multiplex networks have revealed insights into how the brain reorganizes itself in time during a learning task [25], model the cross-frequency dynamics of brain networks [26], and explore its structure-function relationship [27].

This type of modelling is important as brain networks are not random but organized and efficient at both local and global scales [28–30]. To capture the complex interactions between brain regions, their topology, and how these networks dynamically change and reorganize in time, community detection algorithms are employed [23]. The aim of such approaches (such as modularity maximization) is to segregate the network into communities or modules (groups of nodes), where connections within modules are more dense, to describe the underlying organization of the system. Modularity has been explored extensively for many single-layer biological networks, and in how these evolve and adapt due to age or disease [31]. For instance, modularity has been shown to increase along the disease spectrum of AD [32]. This resting-state fMRI (rs-fMRI) study found that changes in key network metrics, and prominently modularity, indicate a reduced ability to integrate information distributed across brain regions and in between module communication as a result of AD. In addition, modularity was highlighted as a more sensitive network measure to MCI and AD than other more frequently used measures like clustering coefficient and path length [32]. However, the extension of modularity from single to multiplex networks was only achieved recently, and thus has seen less study [33].

Importantly, modularity in single and multiplex networks has been exclusively studied at a *global* scale. It is not fully understood how individual regions of a network, such as the brain, change in modularity due to disease, cognitive task phase, or dynamically change in time. Parra *et. al.* showed that not only did the VSTMBT require specific memory binding regions, but also interacting and/or overlapped brain Regions of Interest (ROIs) for object recognition [34]. While global measures of modularity could allow us insight into the overarching structure of the VSTMBT, it is the extent that these individual ROIs interact and work together that is not well understood. As such, we hypothesized that a novel extension of modularity to individual ROIs, and applied to a multiplex framework, would yield novel insights into the regional modularity of the VSTMBT and how an ROI's contribution to modularity

changes as a result of AD.

Here, we introduce a novel measure of nodal group structure for both single and multiplex networks called nodal modularity (nQ). We explore this measure in DTI and for the two phases of the VSTMBT in fMRI and compare the groups – control, early MCI, MCI, MCI converters – comprising the early stages of AD. We construct a multiplex network for the stages of each task and explore the changes in disease states for individual regions of the brain using nQ . These results are compared to single-layer models of fMRI and DTI, random and stochastic block model (SBM) null models, and other multiplex nodal measures of group structure. We find that statistically significant changes in nQ increase with disease severity. Specifically, with increasing number of identified ROIs, which are detected with high sensitivity and specificity along with increasing effect sizes and lower p-values. This effect was most dramatic when comparing MCI and MCI converters, indicating that nQ may have potential in categorizing and detecting this important turning point of AD. Additionally, ROIs that presented with abnormal nQ followed classical trajectories of tau deposition in AD, and showed connection to the deposition of amyloid- β in poor memory binders in the encoding phase (where binding occurs) of the task but not as conclusively in the probe phase as expected. Though our sample size is small, these findings were consistent for both our fMRI and DTI networks and only seen for the binding task and not in shape only, agreeing with prior understanding of the VSTMBT. In sum, nQ not only shows great potential in categorizing and detecting the stages of AD and specifically in separating MCI from MCI converters, but also in improving our understanding of granular changes in community function and structure due to diseases such as AD. Please see S1 Appendix for the code and data availability for this study.

Materials and methods

Participants

Participants were recruited from the Psychology Volunteer Panel at the University of Edinburgh, volunteers from the Scottish Dementia Clinical Research Network interest register, and referrals by old age psychiatrists based at the NHS Lothian and NHS Forth Valley. Eligibility followed from a variety of criteria such as an age over 55, no neurological or psychiatric diseases effecting cognitive function, and normal or corrected to normal vision [11].

A longitudinal study assessed participants with a battery of neuropsychological tests commonly used to assess dementia, such as the Addenbrooke’s Cognitive Examination Revised (ACE-R) and the Hopkins Verbal Learning Test Immediate Total and Delayed Recall, and a novel VSTMBT, grouping subjects into early Mild Cognitive Impairment (early MCI), MCI, and those who converted to Alzheimer’s disease after a 2-year follow up (MCI converters). Further information on this dataset is available here [11].

From these subjects, a subset underwent fMRI (during which they performed the VSTMBT) and DTI tractography scanning. Refer to Table 1 for those who met this criteria and passed pre-processing requirements detailed in the following fMRI and DTI sections. For insight into the neuropsychological tests completed and a statistical analysis of these variables between disease groups see S6 Table.

Table 1. Demographic variables of MCI patients and healthy controls at initial screening. After a 2-year follow up, 6 MCI subjects had converted to AD.

	MCI (N = 16)	early MCI (N = 7)	Healthy Controls (N = 8)
	$M \pm SD$	$M \pm SD$	$M \pm SD$
Age	74.81 ± 6.09	79.71 ± 5.82	79.5 ± 5.15
Years of Education	12.81 ± 3.54	16.57 ± 3.91	15.0 ± 3.54
Sex	9 men; 7 women	5 men; 2 women	2 men; 6 women

Note: N = Number of subjects; M = Mean; SD = Standard deviation.

Anova results on Age: $F(2,28) = 2.62$, $p = .09$, $\eta^2p = .15$

Anova results on YoE: $F(2,28) = 2.86$, $p = .07$, $\eta^2p = .17$

Visual Short-Term Memory Binding Task

Two tasks were explored in our study using non-nameable shapes and non-nameable colours derived by Parra *et al.* [14]. We refer to the first task as shape, where only the shapes are presented to the subject. The second we call Binding, where coloured shapes are presented to the subject. In both cases, the experimental procedure follows as in Fig 1.

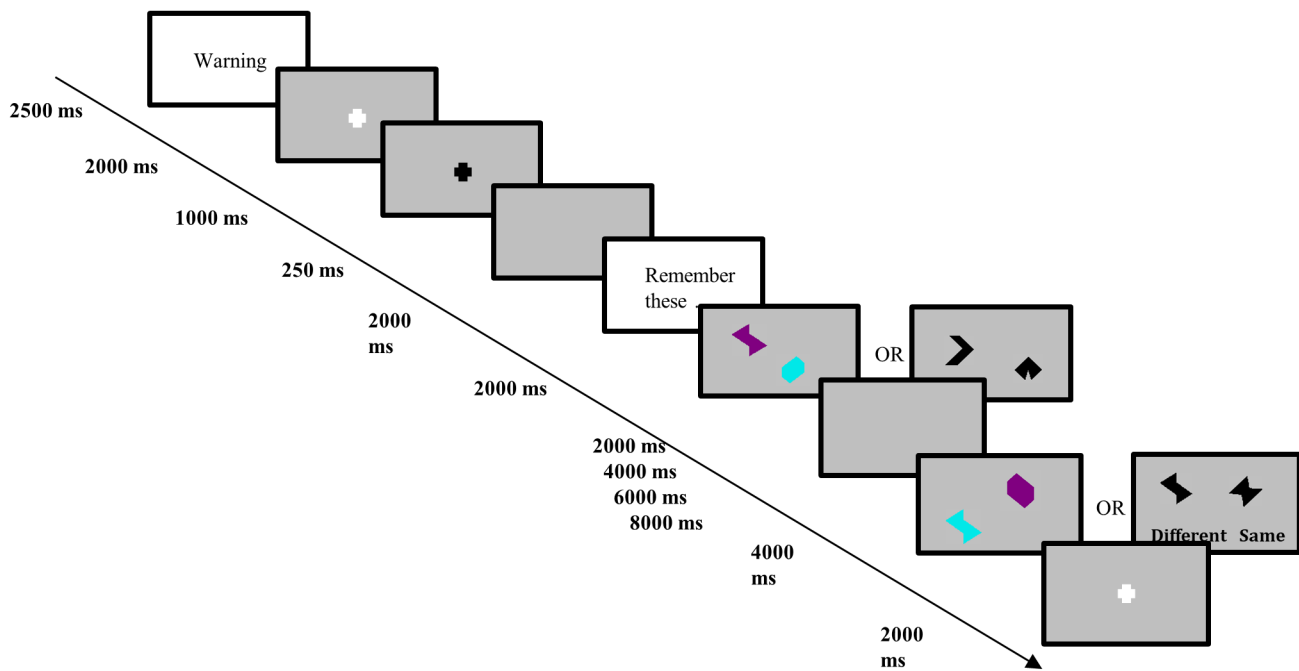


Fig 1. Task procedure. Trials were conducted as follows. A warning screen for 2500ms, a fixation period of 3000ms where a white cross turns from white to black, a blank grey screen for 250ms, a reminder of the instructions for 2000ms, the shapes or shapes with colours (depending on shape or binding task) are displayed for 2000ms (encoding phase), a blank grey screen is displayed for a variable time of (2000, 4000, 6000, or 8000ms) due to the fMRI design optimisation [34] (maintenance phase), a second set of shapes or shapes with colours are displayed for 4000ms (probe phase), and lastly an inter-trial interval of 2000ms. Repeat.

During the probe phase of the procedure, subjects would click a button in either their left or right hand indicating whether or not they believed that the new set of shapes/coloured shapes were different or the same (in 50% of the trials the new set of shapes/coloured shapes would be different). Trials in which the subjects made an incorrect choice were omitted from our analysis as they could stem from lack of engagement or attention. Correct trials were more consistent in capturing the underlying cognitive processes of the VSTMBT due to greater participation with the task itself.

DTI

Diffusion MRI (dMRI) data were collected at the University of Edinburgh Brain Research Imaging Centre (<https://clinical-sciences.ed.ac.uk/edinburgh-imaging>) through a GE Signa Horizon HDxt 1.5T clinical scanner: 3 T_2 -weighted ($b = 0\text{s mm}^{-2}$) and sets of diffusion-weighted ($b = 1000\text{s mm}^{-2}$) single-shot spin echo-planar (EP) volumes acquired with diffusion gradients applied in 32 non-collinear directions. Subsequent volumes were acquired in the axial plane (fov = $240 \times 240\text{mm}$; matrix = 128×128 ; thickness = 2.5mm), giving voxel dimensions of $1.875 \times 1.875 \times 2.5\text{mm}$. The repetition and echo times were 13.75s and 78.4ms, respectively. A T_1 -weighted inversion-recovery prepared fast spoiled gradient-echo (FSPGR) volume was also acquired in the coronal plane with 160 contiguous slices and 1.3 mm^3 voxel dimensions.

This volume was parcellated into 85 ROIs with the Desikan-Killiany atlas with additional regions acquired via sub-cortical segmentation: accumbens area, amygdala, caudate, hippocampus, pallidum, putamen, thalamus, ventral diencephalon, and the brainstem. This volumetric segmentation and cortical reconstruction was performed with FreeSurfer (FreeSurfer, <http://surfer.nmr.mgh.harvard.edu>) using default parameters. For further pre-processing detail please refer to Buchanan *et. al.* [35].

Briefly, pre-processing was conducted with the FSL toolkit (FSL, <https://fsl.fmrib.ox.ac.uk/fsl/fslwiki>). dMRI data underwent eddy current correction, diffusion tensors were fitted at each voxel and FA was estimated, skull stripping and brain extraction were performed, cross-modal nonlinear registration was used to align neuroanatomical ROIs to diffusion space, and the tractography was based on the probabilistic method and white matter seeding approach as in [35].

Of note, the DTI weighted networks were constructed using the streamlines connecting each pair of the 85 grey matter ROIs. The weights of these edges were determined using the mean FA along the interconnecting streamlines [35].

Task-fMRI

fMRI data was collected during the same appointment, acquisition protocol and with the scanner outlined in the prior DTI section. Once localisation scanning was completed, a structural T_1 weighted sequence was acquired (5 contiguous 5mm coronal slices; matrix = 256×160 ; fov = 240mm ; flip angle 8°). During the VSTMBT, contiguous interleaved axial gradient EPI were collected alongside the intercommissural plane throughout two continuous runs (TR/TE = 2000/40ms; matrix = 64×64 ; fov = 240mm ; 27 slices per volume; thickness = 3.5mm ; gap = 1.5mm). This yielded 9-minutes of scan in total, comprising 534 volumes (the first three volumes were discarded at the start of shape and binding trials). For clarity, this resulted in 267 volumes for each of the shape and binding tasks per subject.

Using SPM8 (SPM, <https://www.fil.ion.ucl.ac.uk/spm/>), fMRI pre-processing follows as in [34]. Outlier detection was used to detect slices with a variance greater than 5 standard deviations [36]. Outlier slices were replaced by an averaged image of

the previous and consecutive scans. These images were removed when constructing the network (0.75% of total scans). To account for movement, realignment of each fMRI image to the mean volume of the scan session through B-spline interpolation was done. Slice-timing correction was completed to account for differences in time when acquiring each voxel signal (temporal sync interpolation). Images were then coregistered to their structural T_1 images. Lastly, normalization to the MNI space was conducted using segmentation parameters and DARTEL diffeomorphic mapping functions [37, 38]. fMRI images were also visually inspected for noise and artefacts and subjects who did not pass inspection were removed from the study.

Functional network construction

We use the modified Desikan atlas obtained for each subject (as in the DTI section) to define ROIs and resampled to fit the voxel dimensions of the fMRI data. This was done with SPM12 using Nearest-Neighbour interpolation to ensure that voxel resizing maintained correct ROI mapping. These atlases were also visually inspected to check for proper fitting. For each ROI, the mean signal time-series was extracted from the fMRI images by taking the average signal across voxels defined by the ROI. This was repeated for each image and ROI across the 9-minute scan resulting in time-series of average brain activity at each of our 85 ROIs.

Next, we apply a 0.06Hz high-pass filter to the signals with a sampling rate of 0.5Hz to match our TR of 2s. This was done to account for fMRI signal drift in the very low frequency range [39], and the choice of 0.06Hz relates to the lowest frequency occurring for our longest task trial of 16s. We chose not to low-pass our signal given that, in some cases, our encoding/maintenance task phase is very fast, and thereby in close proximity to the signal’s Nyquist frequency.

We define two task stages for our network construction – ‘encmaint’ and probe. We define encmaint as a combination of the encoding and maintenance phases of the task described earlier in Fig 1. Due to an encoding phase and TR of 2s, this combination of the two phases improves our construction in two ways. It improves our measure of correlation between brain regions for network construction (higher number of samples) and additionally allows us to capture the peak of the haemodynamic response function (HRF) that occurs approximately 5s after stimuli onset (further details in S2 Appendix and S3 Appendix). The probe phase, described in Fig 1, is shifted forward 2s to decrease the overlap between encmaint and probe phases, improve the capture of peak HRF, while introducing minimal noise from the following inter trial interval.

After defining the task phase windows for each task (binding and shape), we reconstruct our time-series from the repetitions of task phases across the 31 trials. More specifically, the time-series for the probe phase is assembled from the windows corresponding to each probe phase within a trial, in sequential order. The same is done for the encmaint phase. From these time-series, we construct an 85×85 connectivity matrix for each task phase by calculating the Spearman correlation between each ROI pair.

Typically, studies of fMRI brain networks use Pearson correlation in the construction of connectivity matrices. However, it is expected that some noise and outliers may remain in fMRI data. These factors, along with additional pre-processing, task windows which could not be constructed perfectly due to inherent limitations of fMRI or the task itself, and other confounding factors such as those present due to the calculation of the mean time-series of regional data, made us select the more conservative Spearman’s correlation for our analysis due to its robustness to outliers [40], and suitability for non-normally distributed data [40, 41]. We also acknowledge a recent study which discovered brain wide increases in functional connectivity with fMRI scan duration [42]. However, we expect this effect to be minor given that our analysis focuses on

comparisons between subject groups (where this effect is ubiquitous) and reduced by randomized presentations of shape and binding tasks over the course of the scan.

To model the dynamics between the two task windows, we construct a dual-layer matrix from each of the two encmaint and probe matrices as in Fig 2a. This is done by connecting each node in one layer to its spatial replica in the other via an edge. These edges are weighted equally and set to 1 as is standard in prior studies on multiplex brain networks [25, 27, 43]. The choice to use weighted graphs, rather than binary, was due to the preservation of the strength of functional association which is complementary to network organization [44].

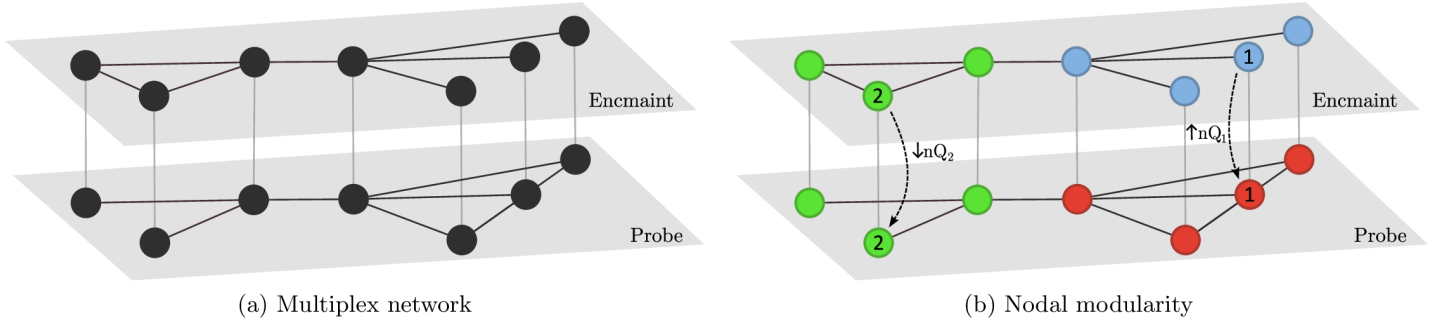


Fig 2. Multiplex network of the VSTMBT. a) Networks for the two task phases of the VSTMBT, encmaint and probe, are constructed from the functional co-activations (correlation in time-series) between all pairs of ROIs. Spatial replicas are connected via an inter-layer edge, as seen in the above figure (light grey edges between the two layers), allowing for continuity of network topology in time. b) Here, multiplex nodal modularity (nQ) has been calculated for each node in our network as in Eq (2) (refer to the following Modularity and Nodal Modularity sections). Each colour represents a separate module (obtained from standard multiplex modularity [33], where modules can exist within a layer (blue and red nodes) or across layers (green nodes). We note that values of nQ are influenced by, but not entirely dependent, on layer and module assignment. For instance, node 2 undergoes a decrease in nQ from the encmaint to probe layer due to a change in topology despite no change in module. Additionally, node 1 undergoes a higher magnitude increase in nQ from the encmaint to probe layer due to changes in topology and module assignment. Not only is it more densely connected in general, but the increase in nQ is driven by the increase in connections existing within a new module (this calculation would be more complex if, for instance, one of node 1’s neighbors in the probe layer was part of the blue module). This example illustrates the interplay between topology, layers, and modules and their effect on nQ . More complex networks, such as those that are weighted, have a greater number of layers and nodes, different across-layer modules, and those with larger topological changes over the layers would result in more complex calculations of nQ . It is the interplay of these elements which determine nQ , and can be interpreted as the importance of a node to the overarching modular structure of the network which, in this case, is governed by topology, modularity, and time.

Modularity

Formally, we define $G = (V, E)$, as a *weighted undirected graph* composed of a finite set of *vertices*, $V = \{v_1, v_2, \dots, v_n\}$, and a two element subset of V called *edges* ($E \subset (v_i, v_j) | v_i, v_j \in V$) [45]. When a pair of vertices share a single edge $(v_i, v_j) \in E$, we say that the two vertices are *adjacent* to each other and that the edge is *incident* to each of our vertices. In addition, we define the *adjacency matrix*, A of our graph G , as the symmetric ($n \times n$) matrix of all vertex pairs where entries $A_{ij} \neq 0$ if $(v_i, v_j) \in E$ and $A_{ij} = 0$ otherwise. Furthermore, we define a *multi-layer network* as a family of graphs $G_s = (X_s, E_s)$ (in our case weighted and undirected), also called *layers*, with $E = \{E_{sr} \subseteq X_s \times X_r; s, r \in \{1, \dots, M\}, s \neq r\}$ as the set of connections between nodes of different layers G_s and G_r with $s \neq r$. The elements of each E_s are called the *intra-layer* (within layer) connections and the elements of each E_{sr} ($s \neq r$) are called

the *inter-layer* (between layer) connections [46]. A *multiplex network* is a type of multi-layer network in which $X_1 = X_2 = \dots = X_M = X$ (all layers have an equal number of nodes) and the only inter-layer connections occur among node replicas, i.e., $E_{sr} = \{(x, x); x \in X\}$ for every $s, r \in \{1, \dots, M\}, s \neq r$. As a reminder, for this study, the entries of A_{ij} are defined by the correlation in fMRI signal time-series between all pairs of brain regions in the case of our functional networks. For our structural networks, entries of A_{ij} are defined by the mean FA of white matter between all pairs of brain regions.

To determine communities within these networks we aim to maximise the modularity quality function (Q) which measures the number of edges that fall within the groups (g_i denotes the group assignment of v_i), minus the expected number of edges that would exist if placed at random [47, 48]:

$$Q = \frac{1}{2m} \sum_{ij} [A_{ij} - \frac{k_i k_j}{2m}] \delta(g_i, g_j). \quad (1)$$

More specifically, for our graph G , we have the sum over all edge weights (A_{ij}) that exist within the same group ($\delta(g_i, g_j) = 1$ when $c_i = c_j$, and 0 otherwise), minus the expected edge weight if edges were placed at random ($\frac{k_i k_j}{2m}$). Here, k_i denotes the degree of v_i , which is the total edge weight of edges incident to v_i and m is the number of edges (sum of edge weights) in G . Q can take on values strictly less than 1, where positive values denote a larger number of edges within groups than by chance, and negative when there are less.

To find the optimal group assignment of nodes such that Q is maximized, we use a Louvain-like greedy method based on [49], the most common method of modularity maximization, due to its extension to multiplex networks [50]. This is done by applying two steps iteratively. 1) We aim to maximise local modularity. To do this we assign each node in the network its own community. Then, for each node, it considers how removing that node from its own community, and adding it to one of the communities it is adjacent to would which result in the maximum positive change in Q . This is repeated iteratively until no individual movement of nodes results in an increase in Q . 2) A new network is built from the communities in step 1, where each community becomes a node, and connections between these newly constructed nodes are defined by the sum of weights between node communities. Then step 1 is applied to this network and iterated until modularity is maximized (and Q is returned along with the group assignment of nodes). It is important to note that this method of modularity maximization (for single and multiplex Louvain), among many others, results in some variation in Q for individual runs [51, 52]. This is due to a variety of factors such as those due to randomized seeding (the initial node community assignment). However, this can be combated by running maximization multiple times as is standard in prior literature [53–55]. We do the same in this study, reaching stability through multiple iterations and in using an iterated version of the algorithm detailed in the following section (similar to consensus clustering [56]). Furthermore, networks in this study are both small and weighted where issues in Q variability is much less severe [51].

While the Louvain method has been defined for both positive and signed networks [31], we choose to consider negative weights as equal to positive weights for modularity maximization. While negative weights have been argued to be neurobiologically relevant [31], interpreting the differences between modules constructed from negative and positive weights separately is not well understood. We worried that per subject differences in the proportion of positive to negative weights could lead to large changes in modularity that would be difficult to interpret. This is particularly important given that we are extending modularity to individual nodes in the following

section.

Nodal Modularity

In network neuroscience, community detection algorithms are often used to obtain a global measure of how modular the network is, how many modules there are, and in multiplex cases, the flexibility of each node (how often a node switches community through the layers of a network) [30]. However, aside from flexibility, the measure of modularity lacks granularity. The use of modularity as a global measure, while useful as a marker of whole brain changes due to disease, fails to capture to what extent these modular subsystems change in time, due to disease, or otherwise.

To tackle this, we extend the standard multislice (multiplex) modularity quality function, $Q_{\text{multislice}}$ [33], to individual nodes as in [57]:

$$Q_i = \frac{1}{2\mu} \sum_{j,r} [(A_{ijs} - \gamma_s \frac{k_{is}k_{js}}{2m_s} \delta_{sr}) + \delta_{ij} C_{jrs}] \delta(g_{is}, g_{jr}) \quad (2)$$

More specifically, we use the multiplex version of modularity (refer to [33]), where we have introduced layers s and r such that A_{ijs} now represents the edge weight between nodes i and j on layer s . Similarly, our random null model is now described for each layer s , $\frac{k_{is}k_{js}}{2m_s}$, but is now modified by the intra-layer resolution parameter, γ_s , which can modify the resolution of communities within each layer. In this paper we set this to the default value of 1 [33] for simplicity. δ_{sr} and δ_{ij} facilitate the calculation of intra-layer and inter-layer edges separately. In this case, $(A_{ijs} - \gamma_s \frac{k_{is}k_{js}}{2m_s} \delta_{sr})$ describes the multiplex version of the observed number of edges minus the expected number for intra-layer edges on each layer. In the case of inter-layer edges, these are handled by C_{jrs} (inter-layer coupling parameter) which is the weight of a node connected to itself across layers s and r . Typically, all inter-layer edges are equal and set to a default value of 1. The inter and intra-layer weights are included in the sum when nodes share group assignment (groups can exist both within and across layers), $\delta(g_{is}, g_{jr})$, and multiplied by $\frac{1}{2\mu}$ where $2\mu = \sum_j r k_{jr}$ which comes from the steady-state probability distribution used to obtain the multislice null model, detailed here [33].

The modularity at each node, Q_i , can then be calculated using an optimized group assignment, defined a priori, such as the general Louvain method. The optimized group assignment is obtained using the iterated version of the multiplex general Louvain algorithm [50]. This follows the same two step iterative process described for single-layer modularity, but now uses the group assignment of nodes as the seed communities for the Louvain method to be reapplied and maximise multiplex modularity. This is done iteratively until there is no change in seed nodes. This further helps to reduce the variability in the algorithm as described previously. It is of note that, in all following mentions of maximised modularity, that we use the aforementioned iterated version of the algorithm with 100 repetitions, choosing the community assignment that corresponds with the highest modularity from those runs. Note that we found modularity to be tightly distributed over each run.

Default settings are used for this, but with the ‘moverandw’ setting where a node moves to a new community when the probability of choosing that move is proportional to the increase in modularity that it results in. This helps to mitigate some of the undesirable behaviour of ordinal multiplex networks discussed in [52].

In this way, we calculate each node’s contribution to global multiplex modularity as

$$Q_{\text{multislice}} = \sum_i Q_i. \quad (3)$$

From now on, we refer to nodal modularity as $nQ = Q_i$, and note that nQ can just as easily be define for single-layer networks. In this case, the expression for multiplex Q_i at the start of this section reduces to

$$Q_i = \frac{1}{2m} \sum_j [A_{ij} - \frac{k_i k_j}{2m}] \delta(g_i, g_j). \quad (4)$$

Additional datasets

To assess nQ 's novelty and behaviour, we explore nQ in two additional datasets. Namely, Zachary's Karate Club and the Nathan Kline Institute-Rockland Sample (NKI-RS) of rs-fMRI and DTI data.

Zachary's Karate Club is a commonly used dataset for exploring community structure in networks [58, 59]. It is a social network modelling the split in a karate club with one leader leaving and forming their own club and taking half of the members with them. In this case, the network's nodes are people and the edges between them denote friendship. Data was accessed and downloaded from <http://konect.cc/networks/ucidata-zachary/>.

The NKI-Rockland cohort is a publicly available dataset containing 196 subjects across lifetime (114 male; age range: 4-89 y.o.) [60] of pre-processed resting state fMRI (rs-fMRI) and DTI data. These were generated at 3T with the following: an acquisition time of 10:55, TR = 2500ms, TE = 30ms, voxel size = 3mm³, and on 38 slices. DTI had an acquisition time of 13:32, TR = 10000ms, TE = 91ms, voxel size = 2mm, and on 58 slices. Each of the connectomes were parcellated into 188 regions of interest using the Craddock atlas. From these, the network edge weights were computed using Pearson correlation and were normalized by the maximum edge weight to the range [0,1]. In the case of DTI, edge weight was determined by the number of fibers that intersected at least one voxel in both the source and target region of interest (ROI) and normalized with the same method as with the fMRI networks. For further information, pre-processing, and access see [61].

Using the provided rs-fMRI and DTI matrices above, we process each subject's data by taking the absolute values of the fMRI connectivity networks and threshold them. Edges with the lowest edge weight were removed until the fMRI network's density matched that of the the subject's corresponding DTI network. Matching densities in this way helps to minimize some modality specific weighting of modularity within a multiplex setting, as fMRI networks are inherently much denser than DTI networks. However, as will be seen in the results, the two modalities retain very different topologies as expected even after matching for density.

Experimental setup

In this section, we outline the methodology used for studying nodal modularity, and how this measure interacts with the stages of disease in our functional and structural networks.

Experiment 1: Verification of nQ

Behaviour of nQ . Initially, we verify the behaviour of modularity for the shape and binding tasks of the VSTMBT. To accomplish this, we compare the modularity (Q) of our shape and binding networks to random and Stochastic Block Model (SBM) surrogate networks. The aim of this experiment is to verify that the VSTMBT exhibits community structure better than random and that Q is similar or higher than a structured surrogate network (the SBM).

For this, we first construct our random networks by taking an edge in our network and randomly rewiring the edge using the Brain Connectivity Toolbox (BCT) [44]. Single-layer Q is then maximized on the randomized shape and binding networks. We also considered the SBM, a variation of the random graph above but with defined community structure. In essence, it takes a defined set of community labels, and a symmetric matrix defining the probability of connections existing between nodes and randomly constructs a network under these conditions [62]. Here, we construct the SBM with freely available code [63] from our shape and binding networks using the group assignment acquired from maximising Q on the non-surrogate networks. In this way we obtain structured, binary, surrogate networks from our shape and binding task. We maximise Q on these single layer networks to compare the modular behaviour between our networks. These results are presented using violin plots (code available here [64]), comparing Q for shape and binding to their random and SBM surrogate networks shown in Fig 3.

Comparison to other nodal graph measures. To explore nQ as a measure, we validate it against several graph measures within three datasets. Specifically, we compare nQ against other measures of nodal community structure: single and multiplex versions of degree, clustering coefficient, and PageRank algorithms. Single-layer versions of these measures were calculated with the BCT.

Degree is a measure of node importance, which is defined as the number of edges adjacent to a node [65]. Nodes with high values of degree are often considered more important or more central within their networks due to the multitude of connections the node has. For multiplex networks, we calculate degree in the same way, but with the addition of inter-layer edges. Furthermore, note that other multiplex versions of degree exist, such as those aggregated across layers [23].

Clustering coefficient is another measure of node importance, measuring the number of triangles for a node in a graph divided by the number of possible triangles that could exist for that node [65]. In essence, it is a measure of how likely a node’s neighbors are to also be connected. For multiplex networks, clustering coefficient is defined differently. In this case, multiplex triangles are described across two layers, with 2 edges of the triangle existing in one layer and the remaining edge existing on the other (defined as a two-triangle). More formally, it is a measure of the ratio of the number of two-triangles and the number of one-triads (3 connected nodes on one layer with 2 edges) for a node. Refer to Eq (22) in [23] for further information.

On the other hand, PageRank captures the behaviour of a random walker traversing the nodes in a network [66]. To calculate the PageRank centrality of a node i we follow two strategies. 1) to jump to a node selected uniformly at random and, 2) to jump to a neighboring node. The PageRank centrality for node i is then defined as the frequency of repeat visits to itself along this random walk. In multiplex networks, the PageRank centrality of a node on one layer influences the centrality on another. In brief, we choose to use the combined multiplex PageRank algorithm defined in [66], where centrality in one layer adds bias to both strategies 1 and 2 in calculating the PageRank centrality of a node in a separate layer.

For each of our tasks, binding and shape (for our controls), we construct a dual-layer network from the enclaint and probe phases. We maximize modularity using the multiplex Louvain-like method and, using this community assignment, we calculate multiplex nQ at each node using Eq (2). Please refer previously to Fig 2b for an example of this process. To validate nQ , we compare this measure to the other multiplex nodal measures of community structure, discussed above, and plot the per node scatter plots with Pearson correlation for these comparisons in Fig 4.

Next, we explore these comparisons for the two other datasets. For the neuroimaging data (NKI-RS), we construct multiplex, dual-layer, fMRI-DTI networks for each subject

by connecting nodes in the fMRI network to their spatial replicas in the DTI network. We maximize Q and calculate nQ in the same way as discussed in the prior paragraph for our dataset, and compare to the same graph measures in Fig 4. The results of the comparisons between nQ and the various graph measures can be seen in Fig 5b.

For Zachary’s Karate Club, we maximize the single-layer version of Q (Eq (1)) using the iterated version of the single-layer version of the Louvain-like method in [50]. We then calculate single-layer nQ (Eq (4)) from the community assignment corresponding to the maximized Q in the previous step. Lastly, we compare the single-layer versions of degree, clustering coefficient, and pagerank to nQ in Fig 5a.

Experiment 2: Validation of nQ

Overview. In this experiment, we detail how comparisons are made between control and disease groups, single and multiplex network constructions, and binding and shape tasks to validate the utility of nQ in the characterisation of MCI.

For each of our subject groups (control, early MCI, MCI, and MCI converters), and for each of our shape (shape only) and binding tasks (coloured shapes), we explore single-layer encaint and probe networks and their corresponding dual-layer network. Furthermore, we construct single-layer DTI networks for each subject.

For all of the above networks, we calculate nQ with the appropriate single or multiplex methods as described previously. We then compare the differences in nQ between control and disease for each network and task using two statistical tests: permutation test and receiver operating characteristic (ROC).

The permutation test is a method of hypothesis testing widely applicable to a variety of use cases [67]. In brief, given two sets of labeled data (such as control and disease), the permutation test computes the test statistic (in our case a two-sided test of the difference of means between the two samples) across many permutations of the labels of the two groups. For each permutation of the labels, we calculate the difference of means between the newly permuted groups and the difference of means for our original group. In total, our p-value is the proportion of sampled permutations where the absolute difference is different from the absolute value of our original observed difference in means. In our study, we calculate p-value with 10000 permutations using code from [68].

The receiver operating characteristic (ROC) is a diagnostic measure of accuracy [69]. ROC plots are a measure of sensitivity vs. specificity, and typically, values of the area under the curve generated this way is a measure between 0.5 (no apparent distributional difference between the two groups of test values) and 1 (perfect separation of the test values of the two groups).

Using the permutation test and ROC, we explore the extent of the differences in nQ between control and the various stages of disease. We do this for each of the models and explore the effectiveness of nQ at categorizing the stages of disease in single vs. dual-layer constructions and binding vs. shape tasks. We do this for each node in our network, comparing the values of nQ for healthy controls to each of our groups (early MCI, MCI, and MCI converters). That is, for each of the previously mentioned networks, we calculate permutation tests in the following way. For each node (brain region), we take the nQ calculated for each subject in the control group, compare the difference in means with the permutation test and the accuracy of the ROC in classifying disease and control groups to obtain the p-value (p), effect size, and area under the curve (AUC) of the ROC. Due to our small sample size, we take a conservative approach, reporting the regions where $p \leq 0.05$ and $AUC \geq 0.7$ as regions exhibiting significant difference in nQ when comparing control and disease groups. Visualizations of these results are given as tables or visualized on a brain mesh using the BrainNet viewer [70].

We perform a similar, per node analysis of our DTI data. Specifically, we explore nQ calculated on our single-layer FA-weighted DTI networks. We do the same group comparisons of control vs. disease with permutation test and ROC as in the previous section, reporting regions where $p \leq 0.05$ and $AUC \geq 0.7$.

Lastly, we explore ROI changes in nQ for early MCI vs. MCI and MCI vs. MCI converters for our fMRI multiplex and DTI single-layer networks. This is done in the same manner as above by calculating the nQ for each of the ROIs in our networks, then comparing the differences in this measure using permutation tests and ROC.

Results and Discussion

In this Section, and following the methodologies described previously, we verify the behaviour of Q for our task-fMRI, perform nQ benchmarking, and apply this measure to our shape and binding task-fMRI and DTI to explore changes in nQ along the AD continuum.

Experiment 1: Verification of nQ

Initially, we verify that Q is behaving as expected for our shape and binding tasks. We compare Q in our shape and binding networks separately, and in random and SBM surrogate networks in Fig 3. Each of the shape and binding networks exhibited better modular structure than random, and similar modularity to our SBM surrogate networks as expected. This verifies that both the shape and binding tasks of the VSTMBT are exhibiting modular structure. Of note is the slightly increased modularity in the SBM surrogate networks. This is likely due to the binary weighting of the surrogate networks leading to more defined group structure. Regardless, the modularity of the fMRI and SBM surrogate networks, along with the significantly improved performance over the random networks, suggests that the functional networks constructed from the shape and binding tasks exhibited group structure as expected.

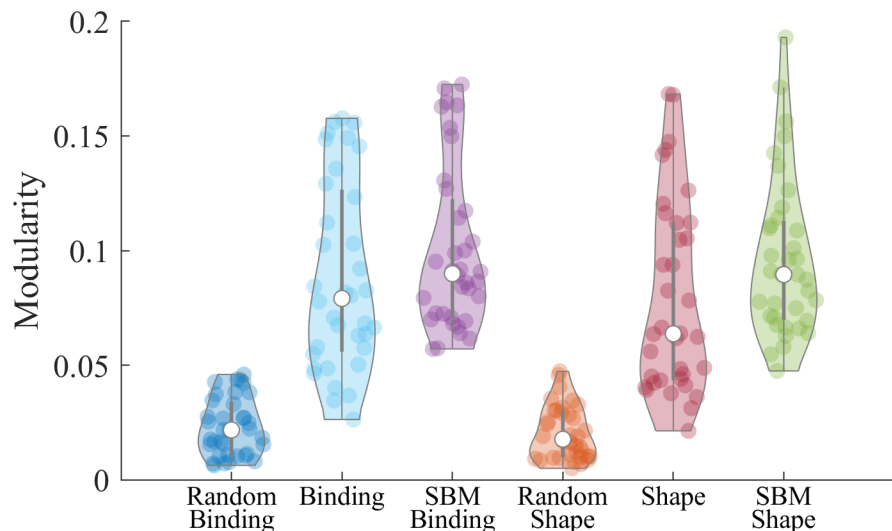


Fig 3. Random and SBM null models for comparisons of modularity in shape and binding tasks: Above are the violin plots of the modularity distribution for shape and binding tasks. This is also explored for our random and SBM surrogate networks.

Next we explore whether nQ is capturing distinct information compared to other nodal graph measures for our dual-layer fMRI data, for each of our tasks and in two additional datasets, NKI-RS and Zachary’s Karate Club.

For our dual-layer fMRI networks and our cognitively normal subjects, we find that, for the binding task, there are moderate negative correlations between nQ and degree and pagerank (-0.54 and -0.6 respectively), and slight negative correlation with clustering coefficient as seen in Fig 4.

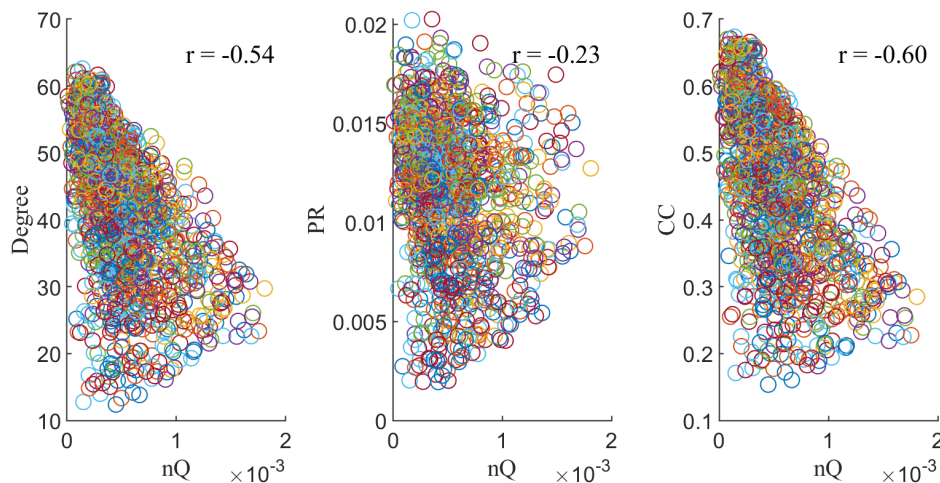


Fig 4. nQ vs. other graph measures: Scatter plots of Degree, PageRank (PR), and Clustering Coefficient (CC) vs. nQ . These measures were calculated in our dual-layer binding task-fMRI networks for cognitively normal subjects.

In Zachary’s Karate club, we find that single-layer nQ is strongly correlated with Degree and PageRank ($r = 0.77$ and $r = 0.78$ respectively), but not with Clustering Coefficient ($r = -0.27$) as seen in Fig 5a.

In NKI-RS, for the rs-fMRI and DTI dual-layer networks, we find a fairly strong correlation ($r = 0.69$) between nQ and degree, while close to no correlation ($r = 0.07$) in PageRank and a moderate negative correlation ($r = -0.53$) in Clustering Coefficient as seen in Fig 5b.

These results point to nQ being a distinct measure of group structure to the other commonly used single and multiplex nodal graph metrics we explored. For Zachary’s Karate club, we found that degree and pagerank were highly correlated with nQ . In Zachary’s karate club, community structure largely centers on the leaders of the two clubs leading to a similarity between the degree of a node and its nQ (contribution to group structure), while PageRank behaving similar to degree in this case could be a result of the network being fairly regular (each node in the network having a similar degree).

On the other hand, for the dual-layer DTI and fMRI networks from the NKI-RS cohort, we saw a fairly strong correlation between degree and nQ with a moderate negative correlation in clustering coefficient. Interestingly, the relationship between nQ and clustering coefficient seems to highlight the difference in modularity between rs-fMRI and DTI. In NKI-RS the modularity of the DTI layer is much higher than the fMRI layer. Therefore, we would expect that the nodes that interact most with the DTI layer rather than the fMRI layer would result in the highest nQ . Since multiplex triangles require integration between both layers, a high multiplex clustering requires strong integration with the fMRI layer which could result in a decreased nQ . This is in contrast to a strongly connected node in the DTI layer with a weak connection to the

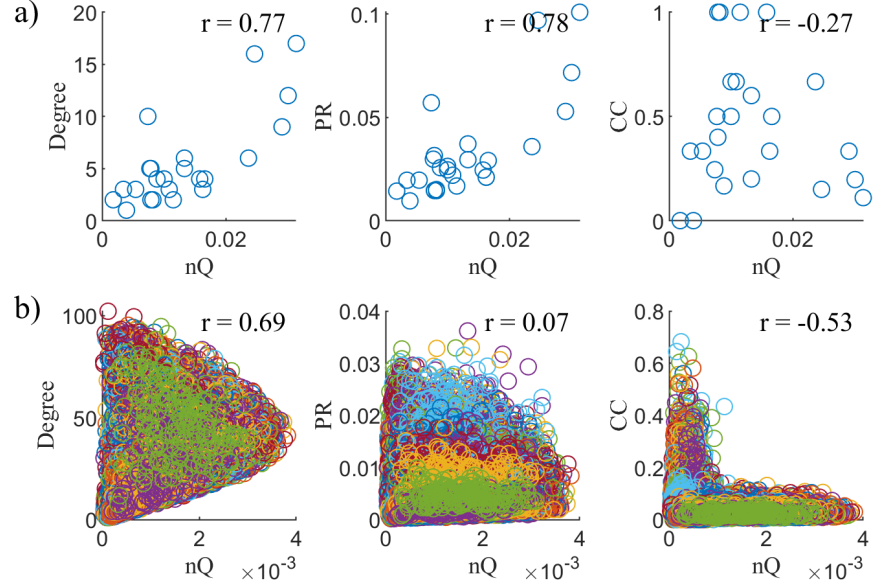


Fig 5. Behaviour of nQ in ZKC and NKI: Scatter plots of Degree, PageRank (PR), and Clustering Coefficient (CC) vs. nQ for Zachary’s Karate club (a) and NKI-RS (b).

fMRI layer resulting in high nQ and low multiplex clustering. This could explain the behaviour seen in CC vs. nQ in Fig 5b.

Lastly, in our dual-layer fMRI networks for the binding task, we saw moderate negative correlations between nQ and degree and clustering coefficient. Unlike our DTI dominated dual-layer networks and sparsely connected social network, our dual-layer fMRI networks are fully connected. Due to this, we expect some high degree nodes to be too densely connected brain wide, rather than specialized to a specific functional grouping (resulting in lower nQ). This reflects the moderate negative correlation ($r = -0.54$) between degree and nQ .

In sum, all three datasets (with single and dual-layer constructions), exhibited different relationships between nQ and the various graph measures. While not an exhaustive list, these tests, along with the formulation of nQ such that $\sum nQ = Q$, add reassurance to the novel behaviour of nQ as a measure for exploring granular group structure in networks.

Experiment 2: Validation of nQ

Here, we explore the changes in nQ across the stages of AD using the previously described permutation test and the area under the curve of the ROC, reporting regions that pass the thresholds of $p \leq 0.05$ and $AUC > 0.7$.

We find that in single and multiplex constructions, for each of the shape and binding tasks, that the number of regions that exhibit statistically significant changes in nQ , increases with disease stage, with the most striking change for control vs. MCI converters in multiplex binding (26 ROIs across enchainment and probe task phases exhibited abnormal nQ) seen in Fig 6c. These regions also exhibit lower p-values (range [0.001 - 0.047]) and greater effect sizes (range [1.019 - 2.363]) and ROC AUC (range [0.788 - 0.979]) as the disease progresses, see Table 2. While these effects were observed for both the shape and binding tasks, and in single and multiplex networks, we focus on reporting the results of the binding task for our multiplex

network model. This is because comparisons in control vs. disease groups resulted in a much higher number of statistically significant changes in regional nQ in both the number of those that pass the permutation test and ROC criteria, but also in the improved performance in lower p-values and higher ROC and effect sizes. This was most prominently seen when comparing Shape and Binding, with some minor improvements for multiplex over single-layer.

Binding and Shape tasks. Parra *et al.* [14] found that when the task demands are adjusted to the patients' capacity, the binding condition was highly sensitive to the disease while performance on the shape only task did not significantly change between controls and familial AD. Our results strongly confirm this behaviour. Not only were there significantly less ROIs that passed our statistical thresholds (6 shape vs. 31 binding ROIs across the stages of disease with poorer p-value, AUC, and effect sizes) comparing the Table for binding (Table 2) to shape (S1 Table), but the most significant changes for shape (in control vs. MCI converters) were also strong results in binding (left lateral and medial orbito frontal). Of note, the medial portion of the orbito frontal cortex has been cited as influential in working memory [71], and a vulnerable region to the early deposition of amyloid- β plaques (a key biomarker of AD) [72, 73].

Single vs. multiplex networks. Additionally, we explore whether modelling the two task phases (encount and probe) as a dual-layer temporal network yields a greater sensitivity to AD. We found that dual-layer modelling identified a similar number of ROIs as its single layer counterpart (26 vs. 25 respectively), but generally improved on the statistical results with lower p-values and higher AUC and effect sizes as seen in S3 Table. This is in agreement with other multiplex temporal network studies which show that multiplex constructions yield insights beyond the analysis of each layer individually [24, 25, 43]. We expect that network models of AD using nQ that were constructed with more layers would see more drastic differences when comparing single and multiplex network constructions.

For further information on the shape and single-layer vs. multiplex results, see S1 Fig, S2 Fig, S1 Table, S2 Table, and S3 Table in Supporting Information.

Neuroanatomical exploration of fMRI. Previously, we hypothesized that since Q has been shown to increase over the stages of AD in fMRI [32], a more granular analysis of AD with nQ would uncover key insights into the disease progression. Additionally, the binding task targets visual memory binding and the temporary retention of complex objects (coloured shapes in this case) and we hypothesized that key ROIs integral to these processes would be impacted, given that the VSTMBT is a cognitive biomarker of AD. Our results reflect this (see Fig 6 and Table 2). We observed that, as AD progressed, there were an increasing number of ROIs that exhibited statistically significant changes in nQ with reduced p-value and increased AUC and effect size (reflecting the ability for nQ to track disease progression as the severity of clinicopathological changes due to AD increase). When considering nQ in the context of graph theory, an increase in nQ can indicate an increased involvement or specialization of a node within its own group and/or a reduction in connections between groups. The neuroanatomical implications of these changes are that of a functional reorganization due to AD. This compensatory response is comprised of a combination of reduced communication between brain subnetworks, and/or increased activity within key brain regions. Such compensatory functional reorganization has been reported in the early stages of AD for both MRI [74] and EEG [75].

We observe these changes in the analysis of control vs. early MCI, MCI and MCI converters and explore the fine grain changes in nQ . We find dysfunction in the limbic, paralimbic, and visual systems. Specifically, the right lingual in early MCI (visual), left and right medial orbito frontal in MCI (paralimbic), into a plethora of dysfunction centered in the limbic, paralimbic, and visual systems in MCI converters - lingual,

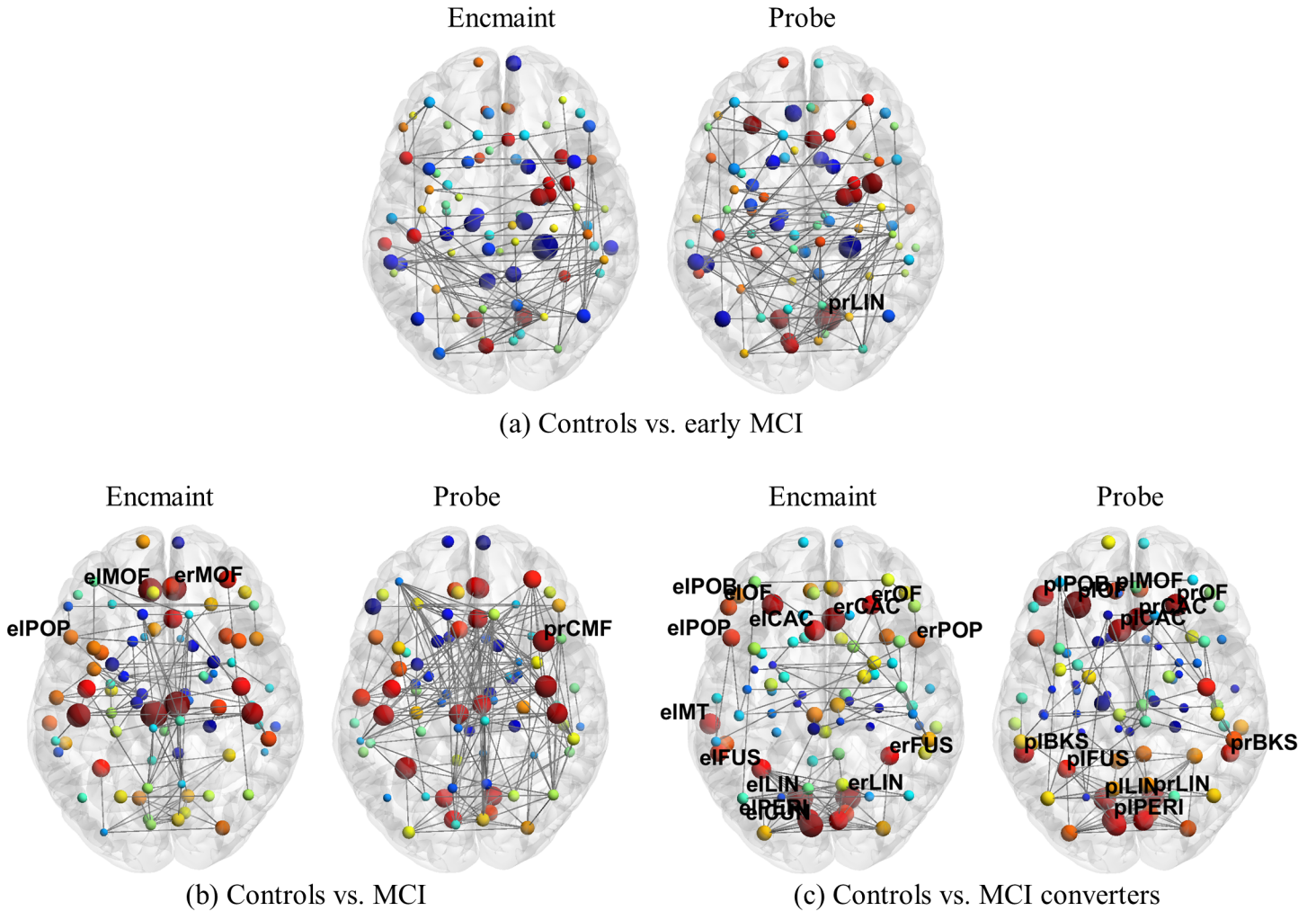


Fig 6. Disease progression for multiplex fMRI binding: Using BrainNet Viewer, we visualize encmaint and probe (left and right brain respectively) layers of our network. Here, nodes in blue represent loss of nQ while those in red represent gains in nQ . The size of the nodes represent the magnitude of this change, while labeled nodes are those that passed the thresholds $p \leq 0.05$ and $AUC > 0.7$. Labels follow the form task phase (e or p), followed by brain hemisphere (l or r), then a shortened version of the ROI (i.e. LIN refers to the lingual). Refer to Table 2 for a more detailed breakdown of the ROIs present in this figure. Furthermore, only 1.5% of edges are visualized for clarity. Note the magnitude of gains in nQ as the disease progresses.

caudal anterior cingulate, lateral orbito frontal, fusiform, cuneus, pericalcarine, and medial orbitofrontal. These functional changes in nQ in the visual, limbic, and paralimbic systems comprise 22/31 (71%) of ROIs identified over early MCI, MCI and MCI converters. This suggests a potential increased activity in visual, limbic, and paralimbic systems and/or reduced communication between these subnetworks and others within the brain. These increases in nQ may be driven by impairments in brain wide communication between or within functional groups as compensation for performance deficits due to AD. Notably, the increases in nQ in the visual, limbic, and paralimbic systems are also common locations for the accumulation of tau and neurofibrillary tangles associated with Braak stages III-IV where MCI typically becomes observable [76]. Additionally, recent research in the VSTMBT suggests that the lingual,

Table 2. fMRI multiplex binding for controls vs. early MCI: This table displays the ROIs which pass the thresholds of $p \leq 0.05$ and $AUC > 0.7$. These ROIs reside in either the enchainment (EM) or probe (P) layers of our multiplex network and in left (L) or right (R) hemispheres of the brain. Standard p-value and effect size is displayed following permutation test and the area under the curve (AUC) of the Receiver Operating Characteristic (ROC).

Controls vs.	ROIs	pvalue	effect size	ROC AUC
early MCI	P R-lingual	0.015	1.452	0.875
MCI	EM L-medialorbitofrontal	0.029	1.147	0.788
	EM R-medialorbitofrontal	0.021	1.144	0.838
	EM L-parsopercularis	0.032	1.134	0.788
	P R-caudalmiddlefrontal	0.047	1.019	0.825
MCI converters	EM R-caudalanteriorcingulate	0.002	2.362	0.938
	EM L-caudalanteriorcingulate	0.006	1.924	0.875
	EM L-lingual	0.007	1.883	0.896
	EM R-lingual	0.010	1.774	0.896
	EM L-middletemporal	0.008	1.708	0.896
	EM L-pericalcarine	0.012	1.659	0.854
	EM R-parsopercularis	0.007	1.634	0.813
	EM R-lateralorbitofrontal	0.006	1.624	0.875
	EM L-parsorbitalis	0.010	1.614	0.875
	EM L-cuneus	0.014	1.556	0.896
	EM L-parsopercularis	0.016	1.483	0.833
	EM L-fusiform	0.020	1.453	0.792
	EM R-fusiform	0.029	1.394	0.813
	EM L-lateralorbitofrontal	0.026	1.149	0.792
	P R-caudalanteriorcingulate	0.001	2.363	0.979
	P L-caudalanteriorcingulate	0.003	2.039	0.917
	P L-bankssts	0.001	1.722	0.958
	P L-lateralorbitofrontal	0.003	1.702	0.917
	P R-lateralorbitofrontal	0.006	1.663	0.896
	P L-parsorbitalis	0.002	1.64	0.938
	P L-pericalcarine	0.012	1.626	0.833
	P R-lingual	0.015	1.531	0.854
	P L-fusiform	0.014	1.453	0.854
	P L-medialorbitofrontal	0.026	1.444	0.813
P R-bankssts	0.027	1.382	0.833	
P L-lingual	0.037	1.29	0.854	

fusiform, middle temporal, pericalcarine, and cuneus are areas of increased amyloid- β deposition in cognitively unimpaired adults with poor memory binding [77], creating a compelling connection between the VSTMBT and a common biomarker of AD. This is especially interesting given that these regions were all seen in the enchainment phase (where binding occurs), but not all in probe (missing the middle temporal, and cuneus) as expected. This connection between amyloid- β deposition and poor memory binding performance may explain some of the increased compensatory functional reorganization ($\uparrow nQ$) in these regions.

It should be noted that, while Braak staging is well described at a population level [78, 79], recent research suggests that there is variation at the individual level and that this trajectory appears to vary along at least four archetypes of tau spread in the brain [78]. We acknowledge this as a limitation and encourage the use of nQ in exploring AD sub-typing and connection to tau deposition in larger, multi-modal,

datasets. Despite this, the connection between observed ROIs with classical tau deposition and amyloid- β remains encouraging. Importantly, we also see a stark difference when comparing controls to MCI and MCI converters (4 vs. 26 ROIs identified). This indicates that nQ might be able to differentiate a crucial turning point of the AD continuum at the individual level.

These results are further supported when looking at early MCI vs. MCI and MCI vs. MCI converters in Fig 7.

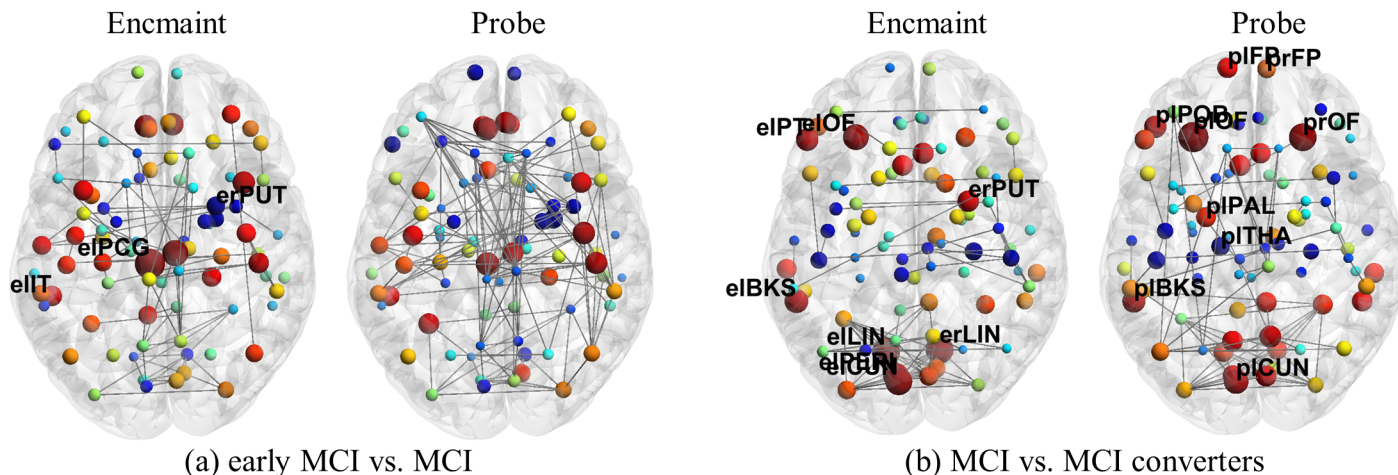


Fig 7. comparisons of nQ for early MCI vs. MCI and MCI vs. MCI converters for multiplex fMRI binding. As in Fig 6, we visualize encmairt and probe (left and right brain respectively) layers of our network. Nodes in blue represent a loss of nQ while those in red represent gains in nQ . The size of the nodes represent the magnitude of this change, while labeled nodes are those that passed our statistical thresholds (details in S4 Table).

Consistent with the previous results, we see the largest changes when comparing MCI to MCI converters (17 ROIs identified and with additional detail in S4 Table). We again see large changes in limbic/paralimbic regions (putamen, pallidum, thalamus, lateral orbito frontal), visual (cuneus, lingual, pericalcarine), and additionally frontal regions (frontal pole). Not only did we observe a similar regional association to tau and amyloid- β deposition as before (expanded to include more brain wide changes such as frontal regions), but also other notable areas in AD progression of putamen, pallidum, and thalamus (regions of the basal ganglia). For instance, an rs-fMRI study [80] found altered functional connectivity density (FCD) between the basal ganglia and other brain structures across the stages of AD, specifically noting reduced long-range FCD for the pallidum (reduced global integration which can lead to an increase in nQ), and general dysfunction in the limbic system. Of note, Valdés Hernández *et al.* [81] had previously reported that structures within the basal ganglia (i.e., the globus pallidus), could be part of the extrahippocampal network supporting VSTMB functions. Interestingly, the thalamus is one of the few regions that decreases in nQ from MCI to MCI converters. Whether this is due to lower task involvement, a reduction in communication with other brain regions in its group, or increased communication between other groups requires further study. Overall, we again predominantly observe an increase in functional reorganization with disease severity, indicating that nQ may assist in locating brain regional changes throughout the disease continuum.

Additionally, we look at these changes in functional connectivity in tandem with changes in white matter micro structure in our DTI networks shown visually in Fig 8 and Table 3.

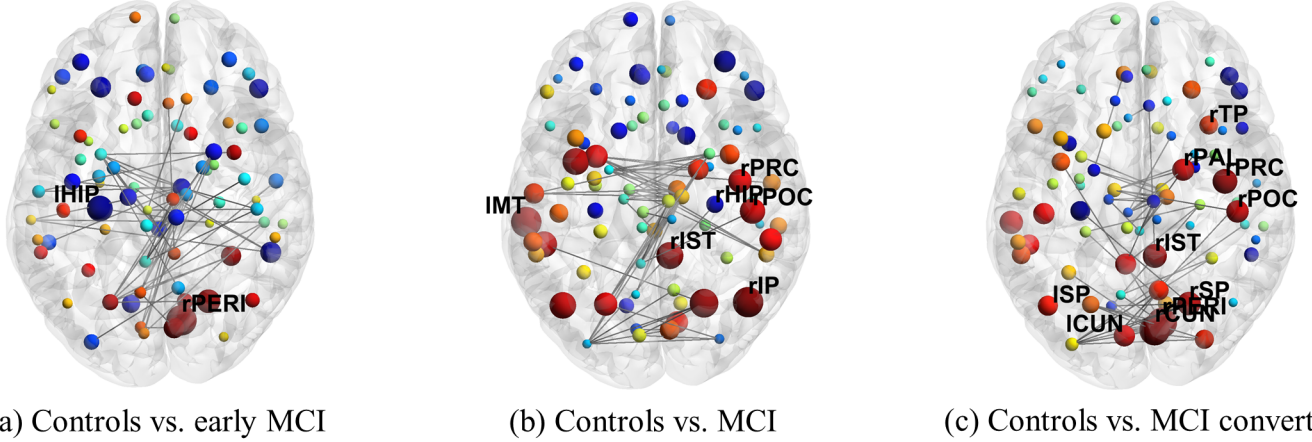


Fig 8. Disease progression for single-layer DTI. As before, blue indicates a loss of nQ while red represents a gain. Here we also see an increase (node size) in nQ as the disease progresses. Furthermore, 1.5% of the network edges are displayed for clarity. Additionally, to reiterate, the DTI networks are constructed based on white matter micro structure. As such, we have a static (no temporal element like in the fMRI networks) single-layer network in this case where the single layer of the network is represented visually by one brain.

Table 3. DTI for control vs. disease This table displays the ROIs which pass the thresholds of $p \leq 0.05$ and $AUC > 0.7$. L and R indicate the left or right hemispheres of the brain respectively. Standard p-value and effect size is displayed following permutation test and the area under the curve (AUC) of the Receiver Operating Characteristic (ROC).

Controls vs.	ROIs	pvalue	effect size	ROC AUC
early MCI	R-pericalcarine	0.048	1.147	0.786
	L-Hippocampus	0.041	-1.183	0.804
MCI	R-postcentral	0.004	1.637	0.863
	R-isthmuscingulate	0.003	1.539	0.888
	R-precentral	0.010	1.415	0.813
	L-middletemporal	0.019	1.230	0.825
	R-inferiorparietal	0.012	1.200	0.888
	R-Hippocampus	0.041	-1.063	0.738
MCI converters	R-cuneus	0.001	2.390	0.958
	R-precentral	0.001	2.046	0.958
	R-superiorparietal	0.002	1.730	0.938
	R-Pallidum	0.014	1.535	0.854
	R-postcentral	0.007	1.504	0.875
	R-pericalcarine	0.026	1.423	0.833
	R-isthmuscingulate	0.018	1.417	0.854
	L-superiorparietal	0.031	1.339	0.875
	L-cuneus	0.042	1.238	0.833
	R-temporalpole	0.038	1.043	0.833

Neuroanatomical exploration of DTI. We find that, like with our fMRI networks and illustrated in Fig 8, that abnormalities in nQ are observed to increase with disease severity (2 in control vs. early MCI, 6 in control vs. MCI, and 10 in control vs. MCI converters), including increases in effect sizes and decreases in p-values. See S5 Table for further detail. Furthermore, we observed some overlap in identified ROIs

(cuneus, pericalcarine, middle temporal which again are all poor binder associated regions of amyloid- β deposition [77]) between fMRI and DTI models when comparing control to MCI converters, but otherwise results were fairly distinct between the two modalities. Notable results are the progression from the medial temporal lobe (hippocampus) and primary visual cortex (pericalcarine) in the earliest stage of disease through to broader areas of brain wide impact through the later stages – consistent with the AD continuum and Braak staging of AD [10, 11, 76]. Additionally, [80] found that Braak staging was associated with reduced FA in many of the regions, and specifically in limbic pathways connecting the medial temporal lobe to subcortical grey matter and medial parietal lobes. Reduction in FA in pathways connecting the medial temporal lobe to the parietal lobe could directly result in increased nQ in these regions, which we observed in the parietal lobe. Such changes have been found in the brains of patients with MCI who are at the highest risk to progress to dementia. For example, Parra *et al.* [17], observed that white matter integrity of the frontal lobe in carriers of the mutation E280A of the PSEN-1 gene [82] correlated with performance when they were assessed with either an associative memory task (i.e., a form or relational binding in long-term memory, see [14] for details) or the VSTMBT. However, a dissociation was observed, with the genu of the corpus callosum accounting for VSTMB impairments and the hippocampal part of the cingulum bundle accounting for long-term memory binding deficits. This suggests that the white matter correlates of VSTMB deficits change as the disease progresses, an observation fully supported by our current findings.

Next we explore comparisons between early MCI vs. MCI and MCI vs. MCI converters for our DTI networks, and as seen in Fig 9.

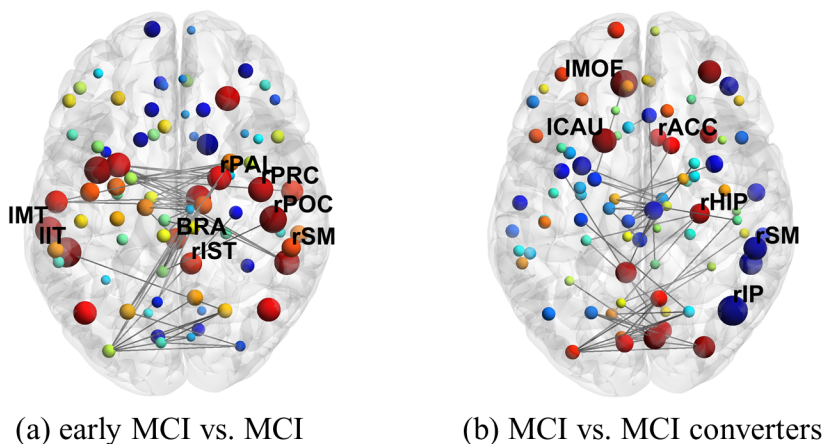


Fig 9. Comparisons of nQ for early MCI vs. MCI and MCI vs. MCI converters for single-layer DTI. Figure generation and details follow from Fig 8. a) Here note the large (node size) increase (red nodes) in nQ in the parietal lobe in the early stages of the disease.

We again see large increases in nQ in the parietal lobe for early MCI vs. MCI (Fig 9a) perhaps pointing to the earlier stages of disease where white matter dysfunction along limbic pathways involving the medial temporal lobe occurs. Additionally, we see involvement of ROIs associated with the basal ganglia when comparing MCI to MCI converters (caudate, accumbens-area) with the addition of the hippocampus. Both of these findings connect to prior discussion on the progression of AD in both DTI and fMRI.

In sum, we see across the stages of AD that fMRI binding and DTI undergo clear

functional and structural reorganization indicated by large increases in nQ . These changes were strongly associated with the trajectory of the AD continuum in deposition of tau and in the connection between poor memory binders and amyloid- β .

Overview. Modularity is a hallmark of the brain. The brain responds to task stimuli by dynamically reorganizing itself in time and compensating for diseases such as AD [31, 32]. However, this reorganization is not fully understood.

To tackle this, we introduced nQ as a method to measure the specific contribution of an ROI to modularity. We explored this measure in the VSTMBT, which is known to require functional activity in specialized and distinct brain regions, along with communication between these regions, to drive cognitive functions such as encoding and retrieval in the brain [34]. We found that changes in nQ were more pronounced and statistically significant with increased disease severity. Specifically, we observed the greatest number of ROIs with abnormal changes in nQ when comparing healthy subjects and MCI patients to those with MCI that converted to AD after a 2-year follow up (Fig 6c, 7b). Additionally, many of these abnormalities in nQ were detected with high sensitivity and specificity (ROC AUC is often $>85\%$ for individual ROIs. Refer to Table 2), and significant p-values with high effect sizes. While this result was most striking in our VSTMBT-fMRI networks, we found distinct differences in MCI and MCI converters in our DTI networks as well (Fig 8c, 9b, and Table 3). Though limited by sample size, these findings present a clear characterization between the stages of MCI, indicating that nQ may be an important measure in predicting and understanding the conversion of MCI to dementia due to AD, especially in combination with the VSTMBT. As changes in modularity are also observed in EEG and MEG [83, 84], future analyses of these granular changes using nQ could not only lead to greater understanding of how functional reorganization occurs in AD, but have the potential in characterizing disease stages in a more widely available imaging modality (EEG).

Conclusion

In neuroimaging, modularity has been largely limited by its use as a global metric. This is despite its utility in describing biological networks, and in its sensitivity to a variety of diseases such as AD. We introduce nQ which novelly extends modularity to individual nodes, thus improving our understanding of how modularity changes at a granular level.

While nQ is applicable beyond biological networks, this study focused on how nQ changes across the stages of AD for DTI white matter microstructure and task-fMRI in visual short-term memory binding. We found that nQ captured the fine grain changes in visual, limbic, and paralimbic functional networks, and were in agreement with tau and amyloid- β deposition for poor memory binders. This trajectory was further supported in our FA-DTI networks where results reflected previously understood changes in white matter connectivity between medial temporal and parietal lobes. Furthermore, nQ was able to distinctly differentiate two key stages of AD (MCI from MCI converters), encouraging further study of nQ as a diagnostic measure of AD. While limited by a small sample size, the results were consistent across single and multiplex constructions, DTI and fMRI, and agreed with previous hypotheses on AD progression and shape and binding tasks. Thus, these results motivate larger studies of nQ in AD, network based analyses of the VSTMBT, and application of nQ to other diseases and networks beyond those biological.

Supporting information

S1 Appendix. Code and data availability. Code to calculate nQ is publicly available at https://github.com/AvalonC-C/Nodal_Modularity. The NKI-Rockland dataset is publicly available with access, study information and pre-processing details given in [61]. Additionally, Zachary’s Karate Club can be accessed at <http://konect.cc/networks/ucidata-zachary/>. Regrettably, data access to our VSTMBT-fMRI cohort (further information here [11]) requires clinical research access approval from NHS Lothian and cannot be shared with any 3rd party as per their confidentiality and disclosure of information policy.

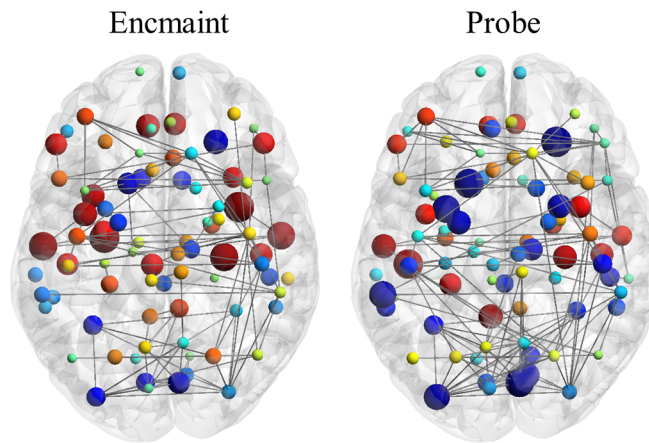
S2 Appendix. fMRI windowing.

During fMRI scanning, stimuli onset does not always line up perfectly with volume acquisition (i.e., a stimuli could be shown at 1.5s while the volume was acquired from 0-2s). We account for this by approximately aligning our encmaint and probe windows to stimuli onset and optimize to capture peak HRF. First, we compare onset of stimulus timings with the following trial and shift our window forward or backward a volume to minimize the offset of trial start and volume acquisition time. This resulted in an offset for our task phase window in the range $[-1.47s, 0.24s]$. We then shift forward our window by one volume (2s), resulting in an offset of $[0.53s, 2.24s]$. The reason to shift forward is to better capture the signal peak of the HRF. To illustrate this shift’s interaction with the HRF, consider the 4s probe phase while accounting for the 2s shift to increase the separation between the two phases. This results in our images corresponding with the signal dynamics of the task from stimuli onset up until a point in the range $[6.53s, 8.24s]$. This ensures that the signal peak information occurring at 5s is captured. It is important to note that there are a very small number of samples that do not perfectly capture the HRF peak. This occurs when the maintenance phase is 2s and the alignment of the task phase window is towards the lower bound of our offset in the range $t = [4.53s, 6.24s]$. Given that the number of cases where our window does not fully capture the HRF peak is very small, and that the offset is only 0.47s, we maintained these samples, acknowledging that in a small number of cases the analysed sample does not fall exactly on the peak of the HRF. This would very slightly reduce our ability to find differences due to stimuli in the encmaint phase of the task but we expect this effect to be minor.

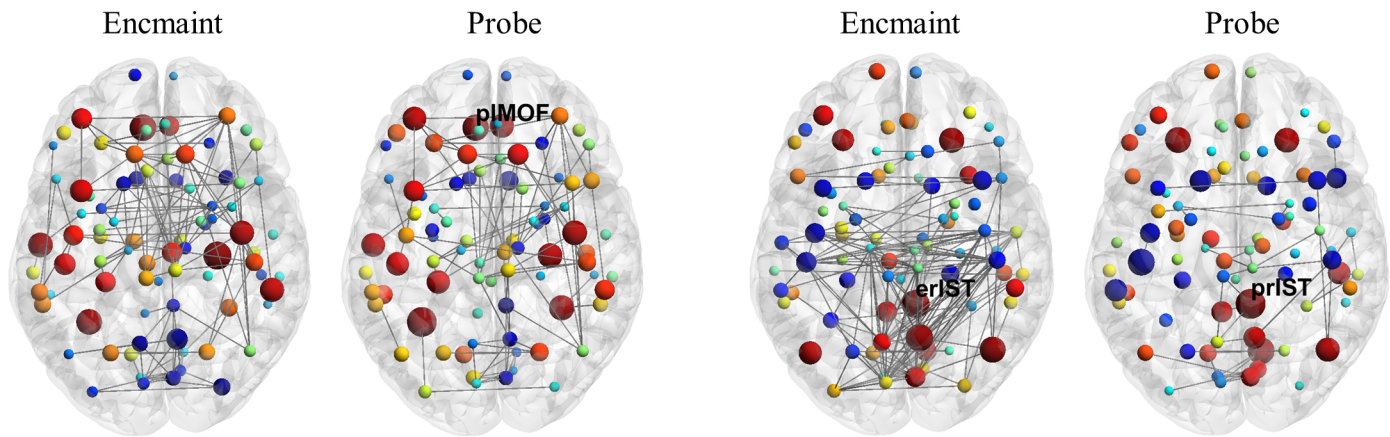
S3 Appendix. Variable maintenance phase of the VSTMBT.

The maintenance phase, where subjects must remember the presented shapes or coloured shapes, is displayed for a variable time as discussed in Fig 1. This is part of the fMRI design optimization aimed at decoupling the BOLD signal from encoding and maintenance for analyses such as statistical parametric mapping (not explored in this study). In this study, we do not expect the variable maintenance window to appreciably influence the comparison of nodal modularity in healthy and diseased brain networks due to the following. First, each subject’s encmaint brain network is constructed from the correlations between repetitions of combined instances of the encoding and maintenance phase preserving temporal variability between brain ROIs. Second, all subjects in the study had an equal number of trials of each maintenance phase length presented at random within the scanning session. This ensures that the total time of all maintenance phases for each subject is equal.

S1 Fig. fMRI disease progression for the shape task. Using BrainNet Viewer, we visualize encmaint and probe (left and right brain respectively) layers of our network. Here, nodes in blue represent a loss of nQ while those in red represent gains in nQ . The size of the nodes represent the magnitude of this change, while labeled nodes are those that passed the thresholds $p \leq 0.05$ and $AUC > 0.7$. Labels follow the form task phase (e or p), followed by brain hemisphere (l or r), then a shortened version of the ROI (i.e. LIN refers to the lingual). Refer to S1 Table for a more detailed breakdown of the ROIs present in this figure. Furthermore, only 1.5% of edges are visualized for clarity. Note the lack of labeled nodes (statistically significant results) in comparison to our binding task (Fig 6).



(a) Controls vs. early MCI



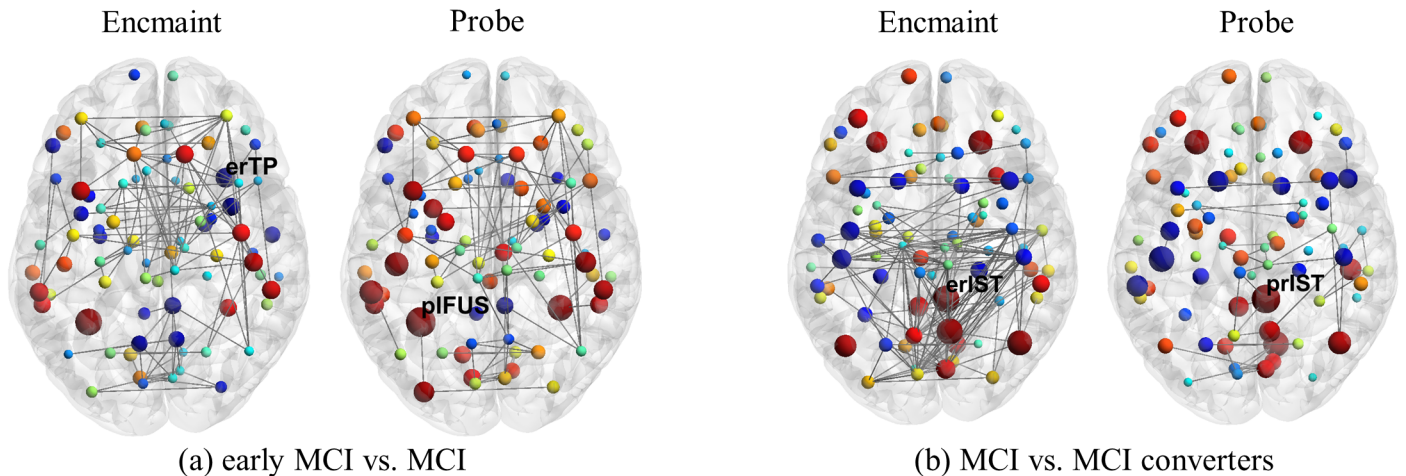
(b) Controls vs. MCI

(c) Controls vs. MCI converters

S1 Table. fMRI disease progression table for the shape task. This table displays the ROIs which pass the thresholds of $p \leq 0.05$ and $AUC > 0.7$. These ROIs reside in either the encmait (EM) or probe (P) layers of our multiplex network and in left (L) or right (R) hemispheres of the brain. Standard p-value and effect size is displayed following permutation test and the area under the curve (AUC) of the Receiver Operating Characteristic (ROC).

Controls vs.	ROIs	p-value	effect size	ROC AUC
early MCI				
MCI	P L-medialorbitofrontal	0.033	1.083	0.800
MCI converters	P L-medialorbitofrontal	0.004	1.830	0.917
	P L-lateralorbitofrontal	0.004	1.740	0.875
	P R-fusiform	0.017	1.406	0.833
	P L-inferiortemporal	0.028	1.302	0.854
	EM L-lateralorbitofrontal	0.046	1.210	0.771

S2 Fig. fMRI progression for early MCI vs. MCI and MCI vs. MCI converters for the shape task. Figure details follow from S1 Fig. For detailed information on ROIs which pass the statistical threshold please see S2 Table. Again, notice the poor results when compared to the binding task (Fig 7).



S2 Table. fMRI progression table for early MCI vs. MCI and MCI vs. MCI converters for the shape task. This table displays the ROIs which pass the thresholds of $p \leq 0.05$ and $AUC > 0.7$. These ROIs reside in either the encmait (EM) or probe (P) layers of our multiplex network and in left (L) or right (R) hemispheres of the brain. Standard p-value and effect size is displayed following permutation test and the area under the curve (AUC) of the Receiver Operating Characteristic (ROC).

Comparisons	ROIs	pvalue	effectsize	ROC AUC
early MCI vs. MCI	E R-temporalpole	0.038	-1.134	0.786
	P L-fusiform	0.040	1.075	0.886
MCI vs. MCI converters	EM R-isthmuscingulate	0.024	1.071	0.833
	P R-isthmuscingulate	0.013	1.055	0.833

S3 Table. Single-layer vs. multiplex results for the binding task and control vs. MCI converters. This table displays the ROIs which pass the thresholds of $p \leq 0.05$ and $AUC > 0.7$. These ROIs reside in either the enclaint (EM) or probe (P) single-layers or modeled together as a multiplex network (results given seperately in the left and right sides of the table respectively). Standard p-value (p) and effect size is displayed following permutation test and the area under the curve (AUC) of the Receiver Operating Characteristic (ROC). While the single and multiplex constructions are similar in the number of ROIs which pass the statistical threshold, note that p-value, effect size and ROC AUC are improved for the multiplex model in almost all cases.

Single-layer				Multiplex			
ROIs	p	effect size	ROC AUC	ROIs	p	effect size	ROC AUC
EM R-caudalanteriorcingulate	0.003	2.067	0.938	EM R-caudalanteriorcingulate	0.002	2.362	0.938
EM R-fusiform	0.006	1.973	0.917	EM L-caudalanteriorcingulate	0.006	1.924	0.875
EM L-lingual	0.008	1.812	0.875	EM L-lingual	0.007	1.883	0.896
EM L-caudalanteriorcingulate	0.009	1.672	0.833	EM R-lingual	0.010	1.774	0.896
EM L-cuneus	0.010	1.608	0.875	EM L-middletemporal	0.008	1.708	0.896
EM R-lingual	0.019	1.537	0.833	EM L-pericalcarine	0.012	1.659	0.854
EM L-pericalcarine	0.024	1.478	0.771	EM R-parsopercularis	0.007	1.634	0.813
EM L-middletemporal	0.021	1.467	0.875	EM R-lateralorbitofrontal	0.006	1.624	0.875
EM R-lateralorbitofrontal	0.020	1.431	0.854	EM L-parsorbitalis	0.010	1.614	0.875
EM L-fusiform	0.026	1.379	0.813	EM L-cuneus	0.014	1.556	0.896
EM L-bankssts	0.036	1.254	0.854	EM L-parsopercularis	0.016	1.483	0.833
EM L-lateralorbitofrontal	0.025	1.129	0.771	EM L-fusiform	0.020	1.453	0.792
P R-caudalanteriorcingulate	0.001	2.191	0.979	EM R-fusiform	0.029	1.394	0.813
P R-lateralorbitofrontal	0.005	1.902	0.917	EM L-lateralorbitofrontal	0.026	1.149	0.792
P L-bankssts	0.003	1.876	0.938	P R-caudalanteriorcingulate	0.001	2.363	0.979
P L-fusiform	0.006	1.778	0.896	P L-caudalanteriorcingulate	0.003	2.039	0.917
P L-caudalanteriorcingulate	0.005	1.769	0.938	P L-bankssts	0.001	1.722	0.958
P L-pericalcarine	0.009	1.763	0.854	P L-lateralorbitofrontal	0.003	1.702	0.917
P L-medialorbitofrontal	0.014	1.619	0.896	P R-lateralorbitofrontal	0.006	1.663	0.896
P L-parsorbitalis	0.008	1.447	0.917	P L-parsorbitalis	0.002	1.64	0.938
P L-lateralorbitofrontal	0.018	1.413	0.875	P L-pericalcarine	0.012	1.626	0.833
P R-lingual	0.025	1.386	0.813	P R-lingual	0.015	1.531	0.854
P R-bankssts	0.029	1.363	0.854	P L-fusiform	0.014	1.453	0.854
P R-precentral	0.036	1.303	0.813	P L-medialorbitofrontal	0.026	1.444	0.813
P L-lingual	0.043	1.242	0.813	P R-bankssts	0.027	1.382	0.833
				P L-lingual	0.037	1.29	0.854

S4 Table. fMRI progression for early MCI vs. MCI and MCI vs. MCI converters for the binding task. This table displays the ROIs which pass the thresholds of $p \leq 0.05$ and $AUC > 0.7$. These ROIs reside in either the enclaint (EM) or probe (P) layers of our multiplex network and in left (L) or right (R) hemispheres of the brain. Standard p-value and effect size is displayed following permutation test and the area under the curve (AUC) of the Receiver Operating Characteristic (ROC).

Comparisons	ROIs	pvalue	effectsize	ROC AUC
early MCI vs. MCI	EM L-inferiortemporal	0.031	1.122	0.786
	EM L-posteriorcingulate	0.046	1.046	0.800
	EM R-Putamen	0.016	-1.331	0.857
MCI vs. MCI converters	EM R-lingual	0.009	1.589	0.833
	EM L-bankssts	0.005	1.582	0.833
	EM L-parstriangularis	0.010	1.552	0.850
	EM L-pericalcarine	0.016	1.443	0.817
	EM L-cuneus	0.014	1.438	0.817
	EM L-lingual	0.027	1.306	0.850
	EM R-Putamen	0.028	1.203	0.750
	EM L-lateralorbitofrontal	0.025	1.123	0.733
	P R-lateralorbitofrontal	0.005	1.645	0.867
	P L-bankssts	0.003	1.525	0.933
	P L-lateralorbitofrontal	0.011	1.428	0.800
	P L-parsorbitalis	0.014	1.315	0.850
	P R-frontalpole	0.029	1.270	0.767
	P L-frontalpole	0.033	1.213	0.817
	P L-cuneus	0.038	1.199	0.733
	P L-Pallidum	0.042	1.177	0.800
	P L-Thalamus	0.030	-1.235	0.850

S5 Table. DTI progression for early MCI vs. MCI and MCI vs. MCI converters. This table displays the ROIs which pass the thresholds of $p \leq 0.05$ and $AUC > 0.7$. L and R indicate the left or right hemispheres of the brain respectively. Standard p-value and effect size is displayed following permutation test and the area under the curve (AUC) of the Receiver Operating Characteristic (ROC).

Comparisons	ROIs	pvalue	effect size	ROC AUC
early MCI vs. MCI	R-postcentral	0.003	1.850	0.929
	R-precentral	0.004	1.729	0.900
	Brain-Stem	0.021	1.262	0.800
	L-middletemporal	0.022	1.238	0.814
	R-isthmuscingulate	0.030	1.195	0.757
	L-inferiortemporal	0.021	1.189	0.886
	R-Pallidum	0.022	1.147	0.871
	R-supramarginal	0.047	1.008	0.757
	MCI vs. MCI converters	L-Caudate	0.033	1.248
L-medialorbitofrontal		0.034	1.238	0.817
R-Accumbens-area		0.046	1.121	0.750
R-Hippocampus		0.034	1.199	0.783
R-inferiorparietal		0.024	-1.182	0.900
R-supramarginal		0.020	-1.248	0.900

S6 Table. Neuropsychological tests.

S6 Table shows the neuropsychological profile of MCI patients, early MCI patients and healthy controls entering the study. ANOVA revealed that patients with MCI performed poorer than healthy controls on ACE [85], MMSE [85], HVLT-DELAY and TOT [86], FAS [87], DIGIT SYMBOL [88], REY-IMMEDIATE and DELAY [89], GNT [90], CLOCK [85], FCSRT-IFR and ITR [91], and TOPF [92]. More specifically, significant differences emerged from comparisons between MCI patients and healthy controls, and MCI patients versus early MCI patients overall. HVLT was carried out poorly from both MCI and early MCI patients compared to the control group, whereas Rey figure delayed copy was significantly underperformed by MCI patients only.

Although the conversion to AD in some patients has been ascertained once the collection of neuropsychological data was done, and MCI converters have not been taken into account here, we can conclude that these results are in line with clinical diagnosis and reflect the progression of the disease through the spectrum.

	MCI (N = 16)			early MCI (N = 7)			Healthy Controls (N = 8)			ANOVA
	M	Mdn	SD	M	Mdn	SD	M	Mdn	SD	E(2,28) (p-value)
	(range)			(range)			(range)			
ACE	77.81	80	11.2	93.42	94	3.4	96.62	96.5	2.72	16.49
	(53-97)			(90-98)			(91-100)			(<0.001)
MMSE	25.06	25.5	3.56	29.14	29	0.9	29.5	30	0.92	9.83
	(17-30)			(28-30)			(28-30)			(<0.001)
TMT-A	71.31	55	66.77	40.85	41	10.76	39.37	40.5	7.23	1.55
	(30-317)			(26-55)			(29-50)			(0.22)
TMT-B	200	160.5	147.21	132.26	131	40.46	100	91.5	39.97	2.42
	(56-585)			(85-191)			(50-171)			(0.1)
HVLT-REC	9.68	10	2.21	10	10	1.63	11.25	12	1.16	1.87
	(4-12)			(7-12)			(9-12)			(0.17)
HVLT-DELAY	2.62	0.5	3.44	4.85	7	3.23	8.87	8.5	2.41	10.36
	(0-10)			(0-8)			(5-12)			(<0.001)
HVLT-TOT	14.56	14.5	6.13	17.28	17	3.9	23	23	4.37	6.37
	(4-29)			(10-22)			(16-29)			(0.004)
FAS	32.62	31.5	16.19	51.57	52	8.1	49.12	50	11.4	6.49
	(9-65)			(41-60)			(31-69)			(0.005)
ANIMAL FLUENCY	6.68	5.5	5.08	6.71	6	3.09	9.12	6.5	7.64	0.57
	(1-12)			(3-13)			(6-28)			(0.56)
DIGIT SYMBOL	36.18	34.5	13.92	56.85	57	7.05	55	53	16.57	8.21
	(10-60)			(48-66)			(35-85)			(0.002)
DIGIT SPAN	5.06	5	0.99	5.57	6	0.78	5.75	6	1.03	1.57
	(3-7)			(4-6)			(4-7)			(0.22)
REY-COPY	32.71	34	3.02	31.42	34	7.43	33.62	34	3.62	0.45
	(24-36)			(15-36)			(25-36)			(.64)
REY-IMMEDIATE	12.25	11.75	8.06	21.5	23	7.65	24.37	26.25	8.33	7.19
	(0-23)			(6-30.5)			(13-34)			(0.003)
REY-DELAY	12.06	14.25	9.13	19.64	20.5	7.49	21.56	19.5	8.45	(3.93)
	(0-24)			(5-30.5)			(10-34)			(0.003)
GNT	18.06	19	4.78	23.57	24	4.19	24.62	26	3.7	7.44
	(7-25)			(17-28)			(18-29)			(0.003)
CLOCK	4.25	4	0.77	4.71	5	0.48	5	5	0	4.36
	(3-5)			(4-5)			(5-5)			(0.02)
FCSRT-IFR	12.18	9.5	10.29	25	24	5.65	26.37	26.5	6.54	9.6
	(0-33)			(17-36)			(15-35)			(0.001)
FCSRT-ICR	13.06	14.5	3.66	15.28	16	1.89	15.87	16	0.35	3.2
	(3-16)			(11-16)			(15-16)			(0.056)
FCSRT-ITR	32.93	38.5	15.78	45.85	48	4.41	47.5	48	1.06	5.37
	(3-48)			(36-48)			(45-48)			(0.01)
TOPF	53.18	56.5	14.5	65.57	70	8.16	65.37	68	5.65	4.32
	(27-70)			(48-70)			(55-70)			(0.02)
GDS	2	1	2.78	1.42	1	1.51	2.21	1	2.53	0.17
	(0-10)			(0-4)			(0-6)			(0.84)

Note: Significant ($p < 0.05$) tests highlighted in bold.

N = Number of subjects; M = Mean; Mdn = Median; SD = Standard deviation.

ACE = Addenbrooke's Cognitive Examination; MMSE = Mini Mental State Examination; TMT = Trail Making Test (Version A and B) [93]; HVLT = Hopkins Verbal Learning Test-Revised (Recognition, Delayed Recall, Total Recall); REY = Rey-Osterrieth Complex Figure Test (Copy, Immediate Reproduction, Delayed Reproduction); GNT = Graded Naming Test; FCSRT = Free and Cued Selective Reminding Test (IFR = Immediate Free Recall; ICR = Immediate Cued Recall; ITR = Immediate Total Recall); TOPF = Test of Premorbid Functioning; GDS = Geriatric Depression Scale [94].

Acknowledgments

Avalon Campbell-Cousins was supported by Edinburgh University's Principle's Career Development PhD Scholarship. The authors also acknowledge the support from the Alzheimer's Society towards the Longitudinal Study of MCI through the Grants AS-R42303 and AS-SF-14-008 awarded to MAP. Additionally, the support of NHS Scotland (both Lothian and Forth Valley boards) in recruiting MCI patients and the Volunteer Panel for healthy controls at the University of Edinburgh.

References

1. Sanford AM. Mild Cognitive Impairment. *Clinics in geriatric medicine*. 2017;33(3):325–337. doi:10.1016/J.CGER.2017.02.005.
2. Gauthier S, Reisberg B, Zaudig M, Petersen RC, Ritchie K, Broich K, et al. Mild cognitive impairment. *Lancet*. 2006;367(9518):1262–1270. doi:10.1016/S0140-6736(06)68542-5.
3. Rossini PM, Di Iorio R, Vecchio F, Anfossi M, Babiloni C, Bozzali M, et al. Early diagnosis of Alzheimer's disease: the role of biomarkers including advanced EEG signal analysis. Report from the IFCN-sponsored panel of experts. *Clinical Neurophysiology*. 2020;131(6):1287–1310. doi:10.1016/j.clinph.2020.03.003.
4. Mueller SG, Weiner MW, Thal LJ, Petersen RC, Jack CR, Jagust W, et al. Ways toward an early diagnosis in Alzheimer's disease: The Alzheimer's Disease Neuroimaging Initiative (ADNI). *Alzheimer's and Dementia*. 2005;1(1):55–66. doi:10.1016/j.jalz.2005.06.003.
5. Zetterberg H, Bendlin BB. Biomarkers for Alzheimer's disease—preparing for a new era of disease-modifying therapies. *Molecular Psychiatry*. 2020;26(1):296–308. doi:10.1038/s41380-020-0721-9.
6. Mahaman YAR, Embaye KS, Huang F, Li L, Zhu F, Wang JZ, et al. Biomarkers used in Alzheimer's disease diagnosis, treatment, and prevention. *Ageing Research Reviews*. 2022;74:101544. doi:10.1016/J.ARR.2021.101544.
7. Grothe MJ, Teipel SJ, Initiative ftADN. Spatial patterns of atrophy, hypometabolism, and amyloid deposition in Alzheimer's disease correspond to dissociable functional brain networks. *Human Brain Mapping*. 2016;37(1):35. doi:10.1002/HBM.23018.
8. Berron D, van Westen D, Ossenkuppele R, Strandberg O, Hansson O. Medial temporal lobe connectivity and its associations with cognition in early Alzheimer's disease. *Brain*. 2020;143(3):1233–1248. doi:10.1093/BRAIN/AWAA068.
9. Bastin C, Delhaye E. Targeting the function of the transentorhinal cortex to identify early cognitive markers of Alzheimer's disease. *Cognitive, Affective, & Behavioral Neuroscience*. 2023;23(4):986–996. doi:10.3758/S13415-023-01093-5.
10. Didic M, Barbeau EJ, Felician O, Tramoni E, Guedj E, Poncet M, et al. Which memory system is impaired first in Alzheimer's disease? *Journal of Alzheimer's disease : JAD*. 2011;27(1):11–22. doi:10.3233/JAD-2011-110557.
11. Parra MA, Calia C, Pattan V, Della Sala S. Memory markers in the continuum of the Alzheimer's clinical syndrome. *Alzheimer's Research and Therapy*. 2022;14(1):1–16. doi:10.1186/s13195-022-01082-9.

12. Dubois B, Feldman HH, Jacova C, Cummings JL, DeKosky ST, Barberger-Gateau P, et al. Revising the definition of Alzheimer's disease: a new lexicon. *The Lancet Neurology*. 2010;9(11):1118–1127. doi:10.1016/S1474-4422(10)70223-4.
13. Dubois B, Feldman HH, Jacova C, Hampel H, Molinuevo JL, Blennow K, et al. Advancing research diagnostic criteria for Alzheimer's disease: the IWG-2 criteria. *The Lancet Neurology*. 2014;13(6):614–629. doi:10.1016/S1474-4422(14)70090-0.
14. Parra MA, Abrahams S, Logie RH, Méndez LG, Lopera F, Della Sala S. Visual short-term memory binding deficits in familial Alzheimer's disease. *Brain*. 2010;133(9):2702–2713. doi:10.1093/brain/awq148.
15. Della Sala S, Parra MA, Fabi K, Luzzi S, Abrahams S. Short-term memory binding is impaired in AD but not in non-AD dementias. *Neuropsychologia*. 2012;50(5):833–840. doi:10.1016/J.NEUROPSYCHOLOGIA.2012.01.018.
16. Supekar K, Menon V, Rubin D, Musen M, Greicius MD. Network Analysis of Intrinsic Functional Brain Connectivity in Alzheimer's Disease. *PLOS Computational Biology*. 2008;4(6):e1000100. doi:10.1371/JOURNAL.PCBI.1000100.
17. Parra MA, Saarimäki H, Bastin ME, Londoño AC, Pettit L, Lopera F, et al. Memory binding and white matter integrity in familial Alzheimer's disease. *Brain*. 2015;138(5):1355–1369. doi:10.1093/BRAIN/AWV048.
18. Kabbara A, Eid H, El Falou W, Khalil M, Wendling F, Hassan M. Reduced integration and improved segregation of functional brain networks in Alzheimer's disease. *Journal of neural engineering*. 2018;15(2). doi:10.1088/1741-2552/AAAA76.
19. Zhang B, Xu Y, Zhu B, Kantarci K. The Role of Diffusion Tensor Imaging in Detecting Microstructural Changes in Prodromal Alzheimer's Disease. *CNS Neuroscience & Therapeutics*. 2014;20(1):3–9. doi:10.1111/CNS.12166.
20. Bassett DS, Sporns O. Network neuroscience. *Nature Neuroscience*. 2017;20(3):353–364. doi:10.1038/nn.4502.
21. van den Heuvel MP, Hulshoff Pol HE. Exploring the brain network: A review on resting-state fMRI functional connectivity. *European Neuropsychopharmacology*. 2010;20(8):519–534. doi:10.1016/j.euroneuro.2010.03.008.
22. Bullmore E, Sporns O. Complex brain networks: graph theoretical analysis of structural and functional systems. *Nature Reviews Neuroscience*. 2009;10(3):186–198. doi:10.1038/nrn2575.
23. Battiston F, Nicosia V, Latora V. Structural measures for multiplex networks. *Physical Review E - Statistical, Nonlinear, and Soft Matter Physics*. 2014;89(3):032804. doi:10.1103/PhysRevE.89.032804.
24. De Domenico M. Multilayer modeling and analysis of human brain networks. *GigaScience*. 2017;6(5):1–8. doi:10.1093/gigascience/gix004.
25. Bassett DS, Wymbs NF, Porter MA, Mucha PJ, Carlson JM, Grafton ST. Dynamic reconfiguration of human brain networks during learning. *Proceedings of the National Academy of Sciences of the United States of America*. 2011;108(18):7641–7646. doi:10.1073/pnas.1018985108.

26. Buldú JM, Porter MA. Frequency-based brain networks: From a multiplex framework to a full multilayer description. *Network Neuroscience*. 2018;2(4):418–441. doi:10.1162/netn.a_00033.
27. Battiston F, Nicosia V, Chavez M, Latora V. Multilayer motif analysis of brain networks. *Chaos: An Interdisciplinary Journal of Nonlinear Science*. 2017;27(4):047404. doi:10.1063/1.4979282.
28. Bullmore E, Sporns O. The economy of brain network organization. *Nature Reviews Neuroscience*. 2012;13(5):336–349. doi:10.1038/nrn3214.
29. Liao X, Vasilakos AV, He Y. Small-world human brain networks: Perspectives and challenges. *Neuroscience & Biobehavioral Reviews*. 2017;77:286–300. doi:10.1016/J.NEUBIOREV.2017.03.018.
30. Betzel RF, Bassett DS. Multi-scale brain networks. *NeuroImage*. 2017;160:73–83. doi:10.1016/j.neuroimage.2016.11.006.
31. Sporns O, Betzel RF. Modular brain networks. *Annual Review of Psychology*. 2016;67:613–640. doi:10.1146/annurev-psych-122414-033634.
32. Pereira JB, Mijalkov M, Kakaei E, Mecocci P, Vellas B, Tsolaki M, et al. Disrupted Network Topology in Patients with Stable and Progressive Mild Cognitive Impairment and Alzheimer’s Disease. *Cerebral Cortex*. 2016;26(8):3476–3493. doi:10.1093/CERCOR/BHW128.
33. Mucha PJ, Richardson T, Macon K, Porter MA, Onnela JP. Community Structure in Time-Dependent, Multiscale, and Multiplex Networks. *Science*. 2010;328(5980):876–878. doi:10.1126/SCIENCE.1184819.
34. Parra MA, Della Sala S, Logie RH, Morcom AM. Neural correlates of shape-color binding in visual working memory. *Neuropsychologia*. 2014;52(1):27–36. doi:10.1016/J.NEUROPSYCHOLOGIA.2013.09.036.
35. Buchanan CR, Pernet CR, Gorgolewski KJ, Storkey AJ, Bastin ME. Test–retest reliability of structural brain networks from diffusion MRI. *NeuroImage*. 2014;86:231–243. doi:10.1016/J.NEUROIMAGE.2013.09.054.
36. Morcom AM, Bullmore ET, Huppert FA, Lennox B, Praseedom A, Linnington H, et al. Memory Encoding and Dopamine in the Aging Brain: A Psychopharmacological Neuroimaging Study. *Cerebral Cortex*. 2010;20(3):743–757. doi:10.1093/CERCOR/BHP139.
37. Ashburner J. A fast diffeomorphic image registration algorithm. *NeuroImage*. 2007;38(1):95–113. doi:10.1016/J.NEUROIMAGE.2007.07.007.
38. Ashburner J, Friston KJ. Computing average shaped tissue probability templates. *NeuroImage*. 2009;45(2):333–341. doi:10.1016/J.NEUROIMAGE.2008.12.008.
39. Smith AM, Lewis BK, Ruttimann UE, Ye FQ, Sinnwell TM, Yang Y, et al. Investigation of low frequency drift in fMRI signal. *NeuroImage*. 1999;9(5):526–533. doi:10.1006/NIMG.1999.0435.
40. de Winter JCF, Gosling SD, Potter J. Comparing the pearson and spearman correlation coefficients across distributions and sample sizes: A tutorial using simulations and empirical data. *Psychological Methods*. 2016;21(3):273–290. doi:10.1037/MET0000079.

41. Bishara AJ, Hittner JB. Testing the significance of a correlation with nonnormal data: Comparison of Pearson, Spearman, transformation, and resampling approaches. *Psychological Methods*. 2012;17(3):399–417. doi:10.1037/A0028087.
42. Korponay C, Janes AC, Frederick BB. Brain-wide functional connectivity artifactually inflates throughout functional magnetic resonance imaging scans. *Nature Human Behaviour*. 2024;8(8):1568–1580. doi:10.1038/s41562-024-01908-6.
43. del Pozo SM, Laufs H, Bonhomme V, Laureys S, Balenzuela P, Tagliazucchi E. Unconsciousness reconfigures modular brain network dynamics. *Chaos: An Interdisciplinary Journal of Nonlinear Science*. 2021;31(9):093117. doi:10.1063/5.0046047.
44. Rubinov M, Sporns O. Complex network measures of brain connectivity: Uses and interpretations. *NeuroImage*. 2010;52(3):1059–1069. doi:10.1016/J.NEUROIMAGE.2009.10.003.
45. Bollobás B. *Modern graph theory*. Springer; 1998.
46. Boccaletti S, Bianconi G, Criado R, del Genio CI, Gómez-Gardeñes J, Romance M, et al. The structure and dynamics of multilayer networks. *Physics Reports*. 2014;544(1):1–122. doi:10.1016/j.physrep.2014.07.001.
47. Clauset A, Newman MEJ, Moore C. Finding community structure in very large networks. *Physical Review E - Statistical Physics, Plasmas, Fluids, and Related Interdisciplinary Topics*. 2004;70(6):6. doi:doi.org/10.1103/PhysRevE.70.066111.
48. Newman MEJ. Modularity and community structure in networks. *Proceedings of the National Academy of Sciences*. 2006;103(23):8577–8582. doi:10.1073/PNAS.0601602103.
49. Blondel VD, Guillaume JL, Lambiotte R, Lefebvre E. Fast unfolding of communities in large networks. *Journal of Statistical Mechanics: Theory and Experiment*. 2008;2008(10). doi:10.1088/1742-5468/2008/10/P10008.
50. Jeub LGS, Bazzi M, Jutla SI, Mucha PJ. A generalized Louvain method for community detection implemented in MATLAB; 2011. Available from: <https://github.com/GenLouvain/GenLouvain>.
51. Good BH, De Montjoye YA, Clauset A. Performance of modularity maximization in practical contexts. *Physical Review E - Statistical, Nonlinear, and Soft Matter Physics*. 2010;81(4):046106. doi:10.1103/PhysRevE.81.046106.
52. Bazzi M, Porter MA, Williams S, McDonald M, Fenn DJ, Howison SD. Community Detection in Temporal Multilayer Networks, with an Application to Correlation Networks. *Multiscale Modeling & Simulation*. 2016;14(1):1–41. doi:10.1137/15M1009615.
53. Bassett DS, Porter MA, Wymbs NF, Grafton ST, Carlson JM, Mucha PJ. Robust detection of dynamic community structure in networks. *Chaos*. 2013;23(1). doi:10.1063/1.4790830/153214.
54. Ashourvan A, Telesford QK, Verstynen T, Vettel JM, Bassett DS. Multi-scale detection of hierarchical community architecture in structural and functional brain networks. *PLOS ONE*. 2019;14(5):e0215520. doi:10.1371/JOURNAL.PONE.0215520.

55. Hanteer O, Magnani M. Unspoken Assumptions in Multi-layer Modularity maximization. *Scientific Reports*. 2020;10(1):1–15. doi:10.1038/s41598-020-66956-0.
56. Lancichinetti A, Fortunato S. Consensus clustering in complex networks. *Scientific Reports*. 2012;2(1):1–7. doi:10.1038/srep00336.
57. Arenas A, Duch J, Fernández A, Gómez S. Size reduction of complex networks preserving modularity. *New Journal of Physics*. 2007;9(6):176. doi:10.1088/1367-2630/9/6/176.
58. Zachary WW. An Information Flow Model for Conflict and Fission in Small Groups. *Journal of Anthropological Research*. 1977;33(4):452–473. doi:10.1086/JAR.33.4.3629752.
59. Girvan M, Newman MEJ. Community structure in social and biological networks. *Proceedings of the National Academy of Sciences*. 2002;99(12):7821–7826. doi:10.1073/PNAS.122653799.
60. Nooner KB, Colcombe SJ, Tobe RH, Mennes M, Benedict MM, Moreno AL, et al. The NKI-Rockland sample: A model for accelerating the pace of discovery science in psychiatry. *Frontiers in Neuroscience*. 2012;0(OCT):152. doi:10.3389/fnins.2012.00152.
61. Brown JA, Rudie JD, Bandrowski A, Van Horn JD, Bookheimer SY. The UCLA multimodal connectivity database: a web-based platform for brain connectivity matrix sharing and analysis. *Frontiers in Neuroinformatics*. 2012;0(NOV):28. doi:10.3389/FNINF.2012.00028.
62. Abbe E. Community Detection and Stochastic Block Models: Recent Developments. *Journal of Machine Learning Research*. 2018;18(177):1–86.
63. Xu KS. MATLAB toolbox for fitting discrete-time dynamic stochastic block models; 2018. Available from: <https://github.com/IdeasLabUT/Dynamic-Stochastic-Block-Model>.
64. Bechtold B. Violin Plots for Matlab, Github Project; 2016. Available from: <https://github.com/bastibe/Violinplot-Matlab>.
65. Fortunato S. Community detection in graphs. *Physics Reports*. 2010;486(3-5):75–174. doi:10.1016/J.PHYSREP.2009.11.002.
66. Halu A, Mondragón RJ, Panzarasa P, Bianconi G. Multiplex PageRank. *PLOS ONE*. 2013;8(10):e78293. doi:10.1371/JOURNAL.PONE.0078293.
67. Good P. *Permutation Tests: A Practical Guide to Resampling Methods for Testing Hypotheses*. Springer Science and Business Media; 2013.
68. Krol LR. *Permutation Test*; 2024. Available from: <https://github.com/lrkrol/permutationTest>.
69. Zweig MH, Campbell G. Receiver-operating characteristic (ROC) plots: a fundamental evaluation tool in clinical medicine. *Clinical Chemistry*. 1993;39(4):561–577. doi:10.1093/CLINCHEM/39.4.561.
70. Xia M, Wang J, He Y. BrainNet Viewer: A Network Visualization Tool for Human Brain Connectomics. *PLoS ONE*. 2013;8(7):68910. doi:10.1371/JOURNAL.PONE.0068910.

71. Barbey AK, Koenigs M, Grafman J. Orbitofrontal Contributions to Human Working Memory. *Cerebral Cortex*. 2011;21(4):789–795. doi:10.1093/CERCOR/BHQ153.
72. Sepulcre J, Sabuncu MR, Becker A, Sperling R, Johnson KA. In vivo characterization of the early states of the amyloid-beta network. *Brain : a journal of neurology*. 2013;136(Pt 7):2239–2252. doi:10.1093/BRAIN/AWT146.
73. Resnick SM, Lamar M, Driscoll I. Vulnerability of the orbitofrontal cortex to age-associated structural and functional brain changes. *Annals of the New York Academy of Sciences*. 2007;1121:562–575. doi:10.1196/ANNALS.1401.027.
74. Parra MA, Pattan V, Wong D, Beaglehole A, Lonie J, Wan HI, et al. Medial temporal lobe function during emotional memory in early Alzheimer’s disease, mild cognitive impairment and healthy ageing: an fMRI study. *BMC Psychiatry*. 2013;13:76. doi:10.1186/1471-244X-13-76.
75. Parra MA, Mikulan E, Trujillo N, Sala SD, Lopera F, Manes F, et al. Brain Information Sharing During Visual Short-Term Memory Binding Yields a Memory Biomarker for Familial Alzheimer’s Disease. *Current Alzheimer research*. 2017;14(12). doi:10.2174/1567205014666170614163316.
76. Braak H, Braak E. Evolution of neuronal changes in the course of Alzheimer’s disease. *Journal of Neural Transmission, Supplementa*. 1998;53:127–140. doi:10.1007/978-3-7091-6467-9_11.
77. Parra MA, Gazes Y, Habeck C, Stern Y. Exploring the Association between Amyloid- β and Memory Markers for Alzheimer’s Disease in Cognitively Unimpaired Older Adults. *Journal of Prevention of Alzheimer’s Disease*. 2024;11(2):339–347. doi:10.14283/jpad.2024.11.
78. Vogel JW, Young AL, Oxtoby NP, Smith R, Ossenkoppele R, Strandberg OT, et al. Four distinct trajectories of tau deposition identified in Alzheimer’s disease. *Nature Medicine*. 2021;27(5):871–881. doi:10.1038/s41591-021-01309-6.
79. St-Onge F, Chapleau M, Breitner JCS, Villeneuve S, Binette AP. Tau accumulation and its spatial progression across the Alzheimer’s disease spectrum. *medRxiv*. 2024;6(1). doi:10.1101/2023.06.02.23290880.
80. Xiong Y, Ye C, Chen Y, Zhong X, Chen H, Sun R, et al. Altered Functional Connectivity of Basal Ganglia in Mild Cognitive Impairment and Alzheimer’s Disease. *Brain Sciences*. 2022;12(11):1555. doi:10.3390/brainsci12111555.
81. Valdés Hernández MC, Clark R, Wang SH, Guazzo F, Calia C, Pattan V, et al. The striatum, the hippocampus, and short-term memory binding: Volumetric analysis of the subcortical grey matter’s role in mild cognitive impairment. *NeuroImage: Clinical*. 2020;25:102158. doi:10.1016/J.NICL.2019.102158.
82. Lopera F, Ardilla A, Martínez A, Madrigal L, Arango-Viana JC, Lemere CA, et al. Clinical features of early-onset Alzheimer disease in a large kindred with an E280A presenilin-1 mutation. *JAMA*. 1997;277(10):793–799. doi:10.1001/JAMA.277.10.793.
83. Jalili M. Graph theoretical analysis of Alzheimer’s disease: Discrimination of AD patients from healthy subjects. *Information Sciences*. 2017;384:145–156. doi:10.1016/J.INS.2016.08.047.

84. De Haan W, Van der Flier WM, Koene T, Smits LL, Scheltens P, Stam CJ. Disrupted modular brain dynamics reflect cognitive dysfunction in Alzheimer's disease. *NeuroImage*. 2012;59(4):3085–3093. doi:10.1016/J.NEUROIMAGE.2011.11.055.
85. Mioshi E, Dawson K, Mitchell J, Arnold R, Hodges JR. The Addenbrooke's Cognitive Examination Revised (ACE-R): a brief cognitive test battery for dementia screening. *International Journal of Geriatric Psychiatry*. 2006;21(11):1078–1085. doi:10.1002/GPS.1610.
86. Benedict RHB, Schretlen D, Groninger L, Brandt J. Hopkins Verbal Learning Test – Revised: Normative Data and Analysis of Inter-Form and Test-Retest Reliability. *The Clinical Neuropsychologist*. 1998;12(1):43–55. doi:10.1076/CLIN.12.1.43.1726.
87. Borkowski JG, Benton AL, Spreen O. Word fluency and brain damage. *Neuropsychologia*. 1967;5(2):135–140. doi:10.1016/0028-3932(67)90015-2.
88. Lafont S, Marin-Lamellet C, Paire-Ficout L, Thomas-Anterion C, Laurent B, Fabrigoule C. The Wechsler Digit Symbol Substitution Test as the Best Indicator of the Risk of Impaired Driving in Alzheimer Disease and Normal Aging. *Dementia and Geriatric Cognitive Disorders*. 2010;29(2):154–163. doi:10.1159/000264631.
89. Rey A, Osterrieth PA. Rey-Osterrieth Complex Figure Copying Test. *Psychological Assessment*. 2011;doi:10.1037/T07717-000.
90. Mckenna P, Warrington EK. Graded naming test: Manual. NFER-Nelson; 1983.
91. Grober E, Buschke H, Korey SR. Genuine memory deficits in dementia. *Developmental Neuropsychology*. 1987;3(1):13–36. doi:10.1080/87565648709540361.
92. Pearson N. Advanced clinical solutions for WAIS-IV and WMS-IV: Administration and scoring manual. San Antonio: The Psychological Corporation. 2009;7.
93. Brown EC, Casey A, Fisch RI, Neuringer C. Trail Making Test as a screening device for the detection of brain damage. *Journal of Consulting Psychology*. 1958;22(6):469–474. doi:10.1037/H0039980.
94. Yesavage JA, Sheikh JI. 9/Geriatric depression scale (GDS) recent evidence and development of a shorter version. *Clinical gerontologist*. 1986;5:165–173.